# Journal Pre-proof

Evolution of the Alu-Dalafilla and Borale volcanoes, Afar, Ethiopia

EmmaJ. Watts, Thomas M. Gernon, Rex Taylor, Derek Keir, Melanie Siegburg, Jasmin Jarman, Carolina Pagli, Anna Gioncada

Please cite this article as: E. Watts, T.M. Gernon, R. Taylor, et al., Evolution of the Alu-Dalafilla and Borale volcanoes, Afar, Ethiopia, *Journal of Volcanology and Geothermal Research* (2018), https://doi.org/10.1016/j.jvolgeores.2020.107094

This is a PDF file of an article that has undergone enhancements after acceptance, such as the addition of a cover page and metadata, and formatting for readability, but it is not yet the definitive version of record. This version will undergo additional copyediting, typesetting and review before it is published in its final form, but we are providing this version to give early visibility of the article. Please note that, during the production process, errors may be discovered which could affect the content, and all legal disclaimers that apply to the journal pertain.

# Evolution of the Alu-Dalafilla and Borale Volcanoes, Afar, Ethiopia

*Emma J. Watts [a*], Thomas M. Gernon [a], Rex Taylor [a], Derek Keir [a,b], Melanie Siegburg [a], Jasmin Jarman [a], Carolina Pagli [c], Anna Gioncada [c]*

[a] School of Ocean and Earth Science, University of Southampton, European Way, Southampton SO14 3ZH, UK

[b] Dipartimento di Scienze della Terra, Università degli Studi di Firenze, Firenze 50121, Italy

[c] Dipartimento di Scienze della Terra, Università di Pisa, Via S. Maria 53, Pisa 56126, Italy.

## ABSTRACT

The Danakil depression marks a progressive change from continental rifting in Afar to seafloor spreading further north in the Red Sea. Extension and volcanism in this incipient spreading centre is localised to the ~70-km-long, 20-km-wide active Erta Ale volcanic segment. Here we combine remote sensing and major element geochemical analysis to determine the structure and composition of three volcanoes on the Erta Ale Volcanic Segment: the Alu dome, the Dalafilla stratovolcano and the Borale stratovolcano. We investigate the evolution and compositional variation within and between these volcanic complexes. Our results show that most flows are sourced from scoria cones and fissures, representing in total 15 phases of volcanism that occurred within four major eruptive stages, most likely occurring in the last 80 thousand years (kyr). The first stage represents large-scale fissure volcanism, comprising submarine basaltic phases. Stage two involves basaltic fissure volcanism around Alu. The third stage is dominated by trachy-andesite to rhyolitic volcanism from the volcano edifices of Alu, Dalafilla and Borale and the fourth by a resumption of small-scale basaltic/trachybasalt fissure systems. Geochemical modelling indicates a paucity of crustal assimilation and mixing within the sub-volcanic magmatic system. Spatial analysis of volcanic cones and fissures within the area indicate the presence of a cone sheet and ring faults. The fissures are likely fed by sills connecting the magma source with the volcanic edifices of Alu and Borale. Our results reveal the cyclic nature of both eruption style and composition of major volcanic complexes in rift environments, prior to the onset of seafloor spreading.

## 1  INTRODUCTION

The East African Rift system (EARS) exposes various stages of rift sector development and thus provides an important natural laboratory to investigate how volcanism varies as continental rifting progresses in maturity towards full seafloor spreading (Wolfenden et al., 2004). Afar is a triple junction between the Main Ethiopian Rift (MER) of the East African Rift system (EARS) to the southwest, the Red Sea Rift to the north, and the Gulf of Aden Rift to the east (Fig. 1; McKenzie et al., 1970). Extension in Afar is localised to volcanic segments (Fig. 1), which mark the currently active plate boundary (Hayward & Ebinger, 1996). The Erta Ale Volcanic Segment (EAVS), located in the southern Red Sea rift of northern Afar (Fig. 1), contains seven volcanoes including Alu, Dalafilla and Borale, all active throughout the Holocene (past 11.7 kyr, Global Volcanism Program, 2013). Despite the volcanic segments being the likely locus of continental rupture, there is a lack of constraints on the geochemistry and timescales of volcanism and how these compare to magmatic segments observed within mid ocean ridges (MORs).
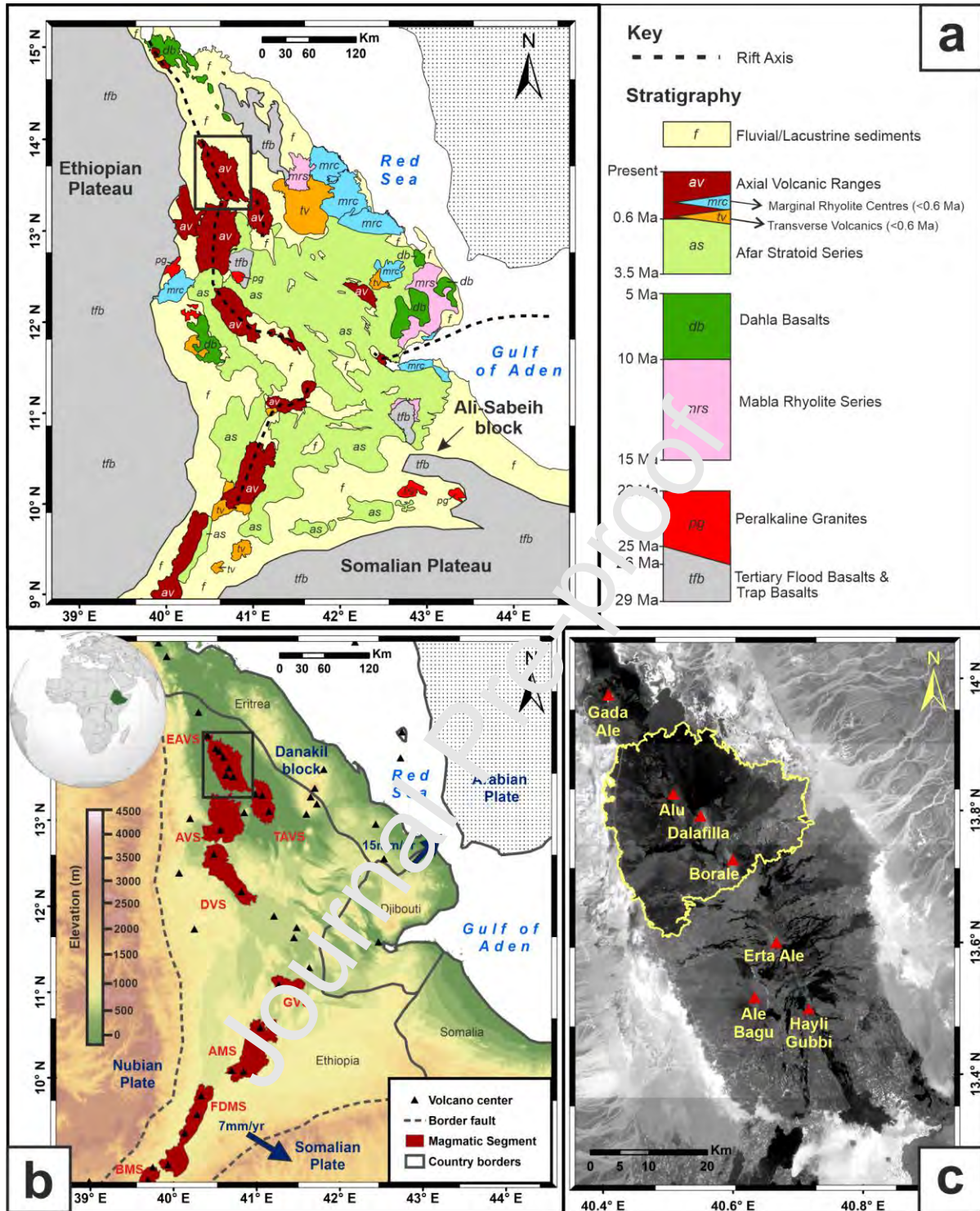
*Figure 1: (a) Geological map of Afar with a stratigraphy of the volcanism in the area (after Beyene and Abdelsalam, 2005). Dark red areas represent the Axial Volcanic Range, also known as volcanic segments which are the loci of current strain and volcanic activity. (b) Left: Map of Afar and the Main Ethiopian Rift (MER). Volcanic segments in Afar and Magmatic Segments in the MER (consistent with literature) are mapped, in red, from north to south: Erta Ale Volcanic Segment (EAVS), Tat'Ale Volcanic Segment (TAVS), Alayta Volcanic Segment (AVS), Dabbahu Volcanic Segment (DVS), Gabillema Volcanic Segment (GVS), Adda'do Magmatic Segment (AMS), Fentale-Dofen Magmatic Segment (FDMS), Boset Magmatic Segment (BMS). Blue arrows indicate plate motion direction and velocity (Ebinger et al., 2008). (c) Right: Map showing the EAVS. The seven volcanic centres are shown by red triangles. The area of this study is outlined in yellow. The imagery shown is Landsat 8 Panchromatic.*

This study focuses on three volcanic centres (Alu, Dalafilla, Borale) in the EAVS in Afar (Fig. 1). We present a detailed geological map and establish a relative chronology of the eruptive history of the volcanoes using a combination of ASTER, Landsat and other satellite images. We combine this information with petrographic and geochemical analyses of 29 lavas and one pumice, collected during the French-Italian field campaign in the 1970s (i.e., Barberi et al., 1973; CNR-CNRS, 1975). These samples were accessed at the "Petroteca Dancalia" repository of Afar rocks housed at the University of Pisa, Italy (http://repositories.dst.unipi.it/index.php/home-afar). These data are combined to explore the evolution of Alu-Dalafilla and Borale, and provide new insights into the spatial and temporal evolution of these volcanic centres. Our results show:

a. the volcanism at Alu-Dalafilla and Borale has been dominated by basalts sourced from fissures orientated making the magmatic segment with a period of more evolved volcanism (e.g., trachyte and rhyolite) sourced from the volcanic edifices (Alu, Dalafilla and Borale).

b. the major element geochemistry for almost all volcanic products can be produced through fractional crystallisation alone with no evidence for crustal assimilation or mixing.

In addition, we provide fundamental new constraints of relative chronology and composition that reduce the uncertainty in their eruptive history. This will guide future radiometric dating strategies and support ongoing hazard and risk assessment in Afar.

## 2   GEOLOGICAL BACKGROUND

### *2.1 AFAR*

Afar is a volcanically and seismically active region located on the junction of three rifts (Field et al., 2012a; Illsley-Kemp et al., 2018a; Illsley-Kemp, 2018b) (Fig. 1a, b). These three limbs are the Red Sea Rift, the Gulf of Aden Rift and the Main Ethiopian Rift (MER) (McKenzie et al., 1970). Afar is bound to the west by the Ethiopian Plateau, the south by the Somalian Plateau, the northeast by the Danakil block and the southeast by the Ali-Sabieh block (Hofstetter & Beyth, 2003, Fig. 1a). The initial opening of the various rifts of the EARS is thought to have occurred diachronously with the Gulf of Aden being the oldest (c. 35 million years ago, Ma; Leroy et al., 2012) and the MER the youngest (c. 15-18 Ma; Wolfenden et al., 2004).

Crustal thickness is broadly a proxy for the degree of extension within the rift (Hutchison et al., 2018), and hence is somewhat linked to the time since rifting began (Hayward & Ebinger, 1996; Ebinger & Hayward, 1996). Crustal thickness values decrease from 35-40 km in the MER (Maguire et al., 2006), to 20-22 km at Dabbahu Volcanic Segment (also known as the Manda Hararo volcanic segment) in Central Afar (Lewi et al., 2016; Hammond et al., 2011), to 16 km at the EAVS in north Afar (Makris & Ginzburg, 1987). Due to the extent of rifting in Afar, compared to the MER, the crust is commonly considered to be proto-oceanic (Hayward & Ebinger, 1996; Pik et al., 1999; Yirgu et al., 2006), making it one of the only places in the world where the continental-oceanic transition is subaerially exposed.

Initial extension in Afar during the late Oligocene (c. 29 Ma) and early Miocene (26 Ma) is thought to have been dominated by normal faulting on steep, ~60-km-long border faults, with the rifting being between the Nubian Plate and Arabian Plate (Wolfenden et al., 2005; Zwaan et al., 2020). The distinct second stage of rifting occurred from 16 – 7 Ma and involved eastward, in-rift, migration of strain and magmatism (Wolfenden et al., 2005). The third stage of Afar's evolution is seafloor spreading style rifting producing 'volcanic segments' (Fig. 1b). These en-echelon zones of

magmatism (e.g., Adda'do, Gabillema, Dabbahu, Alayta, Tat'Ale, Erta Ale) are broadly analogous to those commonly observed in slow-spreading mid ocean ridges (Hayward & Ebinger, 1996; Wright et al., 2006).

The initiation of rifting in Afar is approximately coeval with the peak in emplacement rate of the Ethiopian flood basalts at ~31-29 Ma. The flood basalt province, as a whole, has an estimated volume of ~1 million km$^3$ (Fig. 1a; Hofmann et al., 1997; Wright et al., 2006; Yirgu et al., 2006), with the activity thought to be associated with a mantle plume (White & McKenzie, 1989; Hofmann et al., 1997). The emplacement of the Mablas alkaline to peralkaline rhyolites and basalts occurred at 15 – 10 Ma (Fig. 1a; Vidal et al., 1991), and was followed by the Dalha series (9-4 Ma, Fig. 1a, Vidal et al., 1991). Volcanism occurring between 3.5–0.6 Ma (Thurmond, Abdelsalam & Thurmond., 2006) was dominated by bimodal activity that emplaced a series of basaltic to hawaiite lava flows, including silicic central volcanoes in the upper part, that cover two thirds of the area of the Afar depression (i.e., the Stratoid Series covering approximately 55,000 km$^3$; see Fig. 1a, Lahitte, Gillot & Courtillot., 2003; Corti, 2009). Since then, activity appears to have been dominant at the volcanic segments (Fig. 1, Barberi et al., 1972). Over the past 30 Myr, the proportion of felsic volcanism in the region has decreased and basaltic volcanism has become more dominant (Deniel et al., 1994).

## 2.2 ERTA ALE VOLCANIC SEGMENT

The Erta Ale volcanic segment (EAVS) is in northern Afar (Fig. 1b), and forms a volcanic ridge surrounded by a flat rift floor comprising intercalated clastic sediments, evaporites and lava flows (Bonatti et al., 1971; Barberi et al., 1970, 1972). It forms part of the subaerial southern Red Sea Rift, separating the Nubian Plate from the Danakil microplate. The Danakil microplate rotates anticlockwise from Nubia (Fig. 1), with a rate of extension at Alu-Dalafilla of approximately 12 mm/yr (Acocella, 2006; McClusky et al., 2010; Zwaan et al., 2020).

Barberi & Varet (1970) documented the volcanic history of the EAVS, noting a wide range in compositions of volcanic products from mafic (basalts) to silicic (alkaline rhyolites), but notably the silicic members only constitute ~0.3% of the total volume (Barberi & Varet., 1970). Their observations also indicated the progression in composition was straightforward: from basaltic to silicic with little or no compositional cyclicity. Textural analysis suggested the presence of hyaloclastite textures, taken to indicate a submarine emplacement phase (Barberi & Varet., 1970). However, Barberi & Varet (1970) noted that further refinement of these categories was difficult to perform in the field.

Radiometric dates of volcanic centres within the EAVS are lacking owing to the logistical and political difficulties in accessing and sampling in the area. However, marine reef deposits occur on the edge of the Afar depression in this region, and have been proposed to correspond to the flooding of the Red Sea into the Danakil depression at c. 200 kyr, 120 kyr, and 80 kyr (Lalou et al., 1970). Therefore, on the basis of the lack of visible corals in the EAVS (Barberi & Varet., 1970), the subaerial volcanic deposits of the EAVS are proposed to be post-desiccation (<80 kyr).

The EAVS is an elliptical segment, with lateral extents of ~42 km ENE-WSW and ~90 km NNW-SSE, and comprises seven volcanic centres aligned NNW-SSE (Thurmond, Abdelsalam & Thurmond., 2006; Fig. 1c). The most recent volcanic activity has been detected primarily using satellites (Oppenheimer & Francis, 1997; Venzke, Sennert & Wunderman., 2009; Pagli et al., 2012; Global Volcanism Program, 2013; Moore et al., 2019). Since 2000, the only two centres that have been volcanically active are

Erta Ale: a persistent lava lake with intermittent overflow events and fissural eruption during January 2017 to April 2020 (Field et al., 2012b; Xu, Rivalta & Li., 2017; Moore et al., 2019); and Alu: a fissure eruption to the southeast that occurred in 2008 (Pagli et al., 2012).

## 2.3 ALU-DALAFILLA & BORALE

Dalafilla is a stratovolcano (elevation: 578 m) with a gradient that increases towards the summit; the lower parts of the flanks are of a shallow (~14%) gradient, and the upper section of the flanks are extremely steep (~40% gradient). Alu (395 m) is ellipsoidal in shape, elongated NNW-SSE. The structure and origin of the Alu dome has been long debated with existing hypotheses being that it represents (1) a volcano-tectonic horst (Barberi et al., 1970); (2) a shield volcano (Hagos et al., 2016); and (3) a saucer shaped sill that has resulted in uplift forming the dome shaped topography (Magee et al., 2017).

The 2008 eruptive activity of Alu produced a fissural lava flow (with a volume of 25.4 x $10^6$ m$^3$, Pagli et al., 2012) on the southeast of the dome. Uplift rates of 3 cm per month prior to the eruption was centred over the Alu dome, affecting a region about ~3 km in diameter. To the south of Alu, Dalafilla and Borale did not record any appreciable uplift prior to the eruption, but subsidence was recorded during the eruption south of Alu (Pagli et al., 2012).

Borale consists of two structures, a stratovolcano (elevation 625 m) and a shield volcano composed dominantly of fissural lavas. A'a and pahoehoe lavas have been produced from fissures around Borale, with the oldest deposits being on the eastern side (Barberi et al., 1970). No eruptions have been observed from the stratovolcano of Borale, but fumarolic activity was noted in the field by Barberi & Varet (1970) between 1968 and 1969.

## 3 METHODOLOGY

### 3.1 REMOTE SENSING MAPPING & GEOCHRONOLOGY

Geologic features in the northern part of the EAVS (UTM, WGS 1984 Zone 37N) were mapped using remote sensing data, using observations from Landsat 8 (multispectral, panchromatic and pan sharpened, spatial resolution 30 m, 15 m, and 15 m respectively) alongside Advanced Spacebourne Thermal Emission and Reflection Radiometer (ASTER, spatial resolution 30 m) data. Features mapped include discrete lava flows (and different lava flow sequences corresponding to discrete effusive eruptive phases), volcanic cones, fractures, faults and fissures, as well as possible eruptive vents.

Phases of lava flows are described as a lava flow(s) that occur in similar locations, often sourced from the same fissure or vent, that exhibit similar physical characteristics and are estimated to occur as either a single fissure/rifting episode or multiple but temporally and spatially clustered fissure/rifting episodes. In Afar, single fissure/rifting episodes are observed to last several years (<10 years) (e.g. Erta Ale - Moore et al., 2019 ; Dabbahu - Wright et al., 2012), and fissure/rifting episodes are thought to likely be separated by ~100s of years timescales of quiescence (Wright et al., 2006; Pagli et al., 2015). With these constraints coupled with our observation of 15 phases younger than 80k years, we estimate that our phases likely represent <10s to several 100s of years timescales and separated by several 100s to several 1000s of years timescales.

Stages are defined as groups of phases with similar physical and geochemical characteristics that erupted over a longer period potentially from multiple fissures or vents. We stress that future

radiometric dating is required to determine the chronology associated with each eruptive stage. Similarities are identified based on the temporal and spatial relationships of the phases as well as their geochemical and morphometric characteristics. Various combinations of the 11 electromagnetic spectrum wavelength bands available from Landsat 8 were used to highlight differences between lava flows (see Supplementary Figure SF1).

We determined a relative chronology by assessing cross-cutting relationships (see Supplementary Figure SF1), between the edges of lava flows and any cross-cutting tectonic features. This was aided by the use of Google Earth 3D terrain view, which uses NASA's Shuttle Radar Topography Mission (SRTM) data with a spatial resolution of 30 m.

### 3.2 MORPHOMETRIC ANALYSES

Morphometric analysis of the lava flows provided additional constraints on the eruptive style, activity and extent. We utilised Landsat 8 data to obtain length and area measurements for each eruptive phase. The apparent length and area were measured by tracing the flow path from their (visible) start to end points. The error associated with the length measurements (estimated to be ± 15 m) is dependent on the resolution of the satellite image used. However, the sources of lava flows are often obscured by overlapping flows and hence the area and lengths of lava flows are considered minimum estimates. Numerous thickness measurements were determined from elevation profiles across the edges of flows and the average was calculated for each phase. Subsequently volume estimates were calculated as the product of the average thickness and the total area of the phase ('planimetric' approach; e.g., Stevens et al., 1999) The use of thicknesses measurements from the edge of lava flows could result in an underestimate of the mafic volumes due to the flow centres often being thicker than the edges and an overestimate for felsic volumes due to the edges being thicker than the flow centres.

### 3.3 PETROGRAPHIC ANALYSES

Petrological analysis was performed using optical microscopy. Thin sections were photographed, and the images stitched together using photogrammetry methods using Kolor Autopano Giga 3.7 software. Modal abundances were calculated using JMicrovision point counting software, using 500 point-counts per sample.

### 3.4 GEOCHEMICAL ANALYSES

A representative selection of 30 rock samples (locations illustrated in figure 2 and coordinates provided in table 2), were crushed, soaked and ultra-sonicated in water for 3 hours and subsequently dried at 85°C for 12 hours. The samples were then manually ground using an agate pestle and mortar to avoid contamination from metallic equipment. For each sample, the Loss of Ignition (LOI) was determined by weighing before and after heating at 950°C for two hours. Following this, glass beads used for major element analysis were produced using a mixture of 20% lithium tetraborate and 80% lithium metaborate with the sample (5:1 respectively) on a fluxana gas fusion bead maker. Whole rock analyses were undertaken with the PANalytical Axios-Advanced Xray fluorescence spectrometer at the University of Leicester. Analytical precision and accuracy were monitored by standards BCS375, BCS375, MRG -1, NIM-D, and BCS372/1, and are shown in Supplementary Data file SD1.

# 4 RESULTS

## 4.1 GEOLOGICAL MAP OF ALU-DALLAFILLA AND BORALE – RELATIVE CHRONOLOGY OF LAVA FLOWS

Using a combination of remote sensing techniques (see section 3.1), we constructed a map of the lava flows at Alu-Dalafilla and Borale (Fig. 2). The volcanic activity of the area was divided into four main eruptive stages: (1) rift floor basalts predating the main volcanic edifices of Alu, Dalafilla and Borale; (2) fissure basalts around Alu-Dalafilla; (3) point source volcanism from all three volcanic centres; (4) rejuvenated fissures around Alu-Dalafilla. The four stages can be further sub-divided into 15 eruptive phases (A to O; Figs. 2, 3), defined as eruptions that are spatially and temporally clustered and that appear to be of similar style. In total, 92 lava flows were mapped, excluding the rift floor lavas (phase A; Fig. 2). The flows were assigned to a phase based on their relationship with surrounding flows, their textural characteristics, and their location.

We also mapped the major faults in the area (Fig. 4). These appear to be centred around the major volcanic centres, in particular the Alu Dome (Fig. 4a) and Borale shield (Fig. 4b), and to the west of Dalafilla (Fig. 4c). The Alu dome is dominated by a conjugate fault pattern (NNW-SSE and ENE-WSW) with one dominant direction (NNW-SSE) broadly parallel to the main rift and fissures within the area (Fig. 4a). Further south, the faults follow a NW-SE orientation again sub-parallel to the rift axis and fissures. Borale is unique in the area due to the presence of curvilinear faults (average length 1091 m, range 125 m to 4119 m) with smaller faults (average length 490 m, range 164 m to 1270 m) orthogonal to the curvilinear faults (Fig. 4b).

Mafic volcanic cones (small volume, monogenetic volcanic centres) are abundant within 6 km of the rift axis, with most occurring either 3 km west of the rift axis or on the rift axis itself. More than 200 cones were recorded in an area of 324 $km^2$, giving an average density of 0.672 per $km^2$. On the top of the Alu-dome and Borale, volcanic cones are rare. A series of volcanic cones form arc-like shape surrounding the southwestern side of the Borale shield volcano (Fig. 4b). Cones also radiate around the Alu dome to the north, southeast, and southwest (Fig. 4a).

### 4.1.1. Stage 1: Rift floor basalts

The rift floor basalts are highly weathered, with little flow characteristics remaining making it difficult to differentiate individual eruption events (Figs. 5a, b). This is consistent with the observations of Barberi & Varet (1970), who proposed that they were emplaced in a shallow submarine environment. Phase A is widespread, with an observed outcropping (minimum) area of 218.8 $km^2$ (Fig. 2; Table 1) however, an accurate estimation of the areal extent of Phase A is difficult to perform due to the presence of overlying lava flows. It is possible that Phase A formed a blanket-like lava flow covering the study area (751 $km^2$) and has since been overlain by more recent lava flows.

Phase B, which predates or is contemporaneous with Phase C, is confined to the eastern side of Dalafilla covering a minimum area of 37.8 $km^2$ and was sourced mainly from two eruptive vents (Figs. 2–3; Table 1). Phase C was formed from multiple lavas sourced from a combination of fissures (beneath the Borale shield) and points (to the southwest) covering a minimum area of 80.1 $km^2$ (Figs. 2–3; Table 1). Two flows are sourced from fissures in the region beneath the Borale area. Phase D consists of at least four flows localised around Borale, and two flows at Alu. The source edifice cannot be identified so the vent location may lie beneath the deposits postdating Phase D, near the rift axis. The total area of these phases is 46.8 $km^2$ and 6.8 $km^2$ respectively (Figs. 2–3). The

two areas lack overlapping relationships and are similarly weathered, making their relative timing uncertain.

### 4.1.1. *Stage 2: Fissure basalts around Alu-Dalafilla*

The fissure basalts around Alu-Dalafilla occurred during three phases (E, F, G) with activity progressively migrating clockwise from the southwest of the Alu dome towards the northeast of the dome. Multiple eruption centres of mostly fissures with some volcanic cones are aligned around the
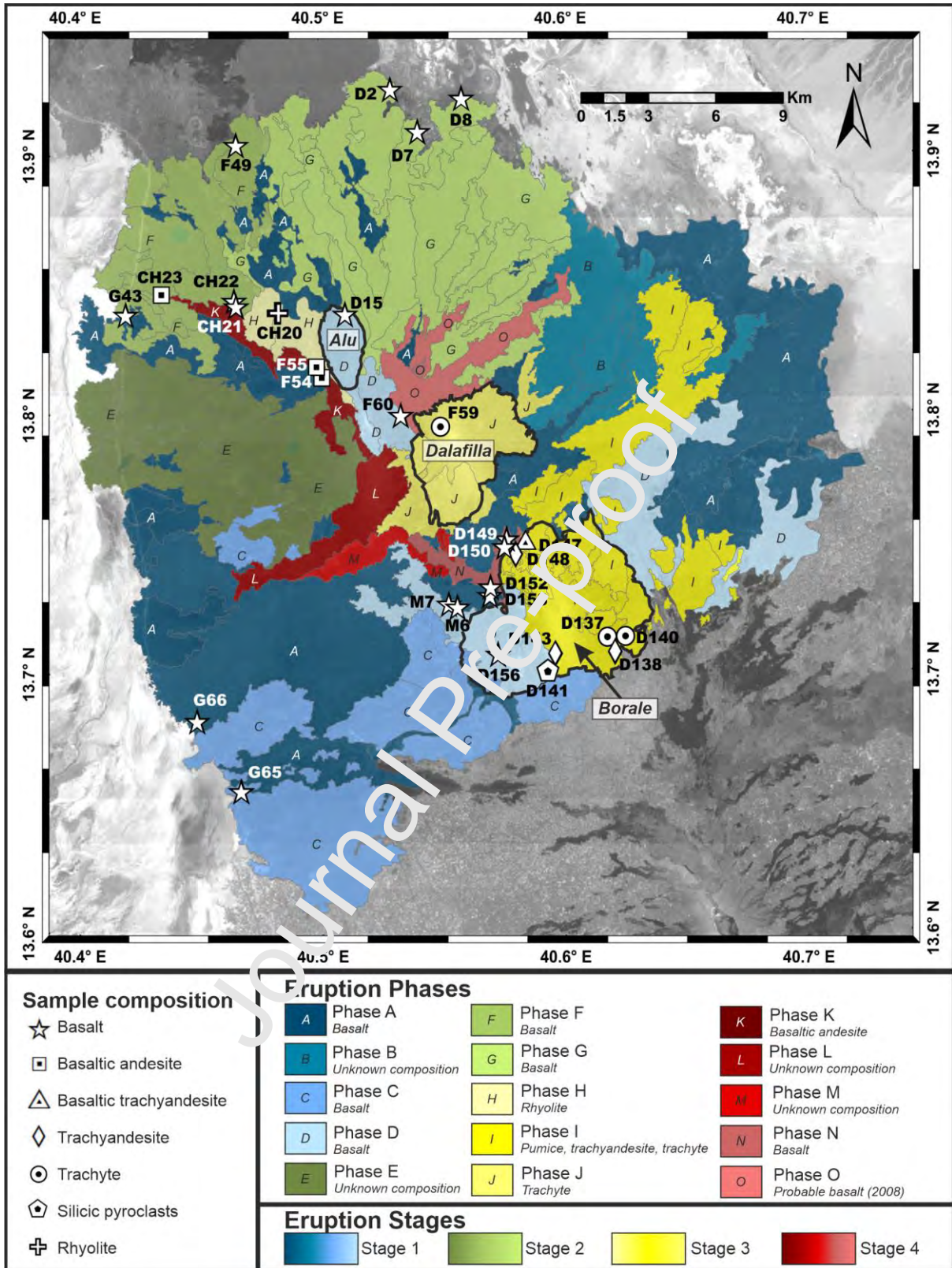
*Figure 2: Map of the northern part of the EAVS including Alu, Dalafilla and Borale. Different colours denote the eruption stages with different shades denoting different phases (Blue – Stage 1, Green – Stage 2, Yellow – Stage 3, Red – Stage 4) as shown in the key. The most recent phase (O) is that of the 2008 eruption. Sample locations and compositions (i.e., those subjected to bulk rock analysis) are shown using symbols. Background imagery is Landsat 8 Panchromatic.*
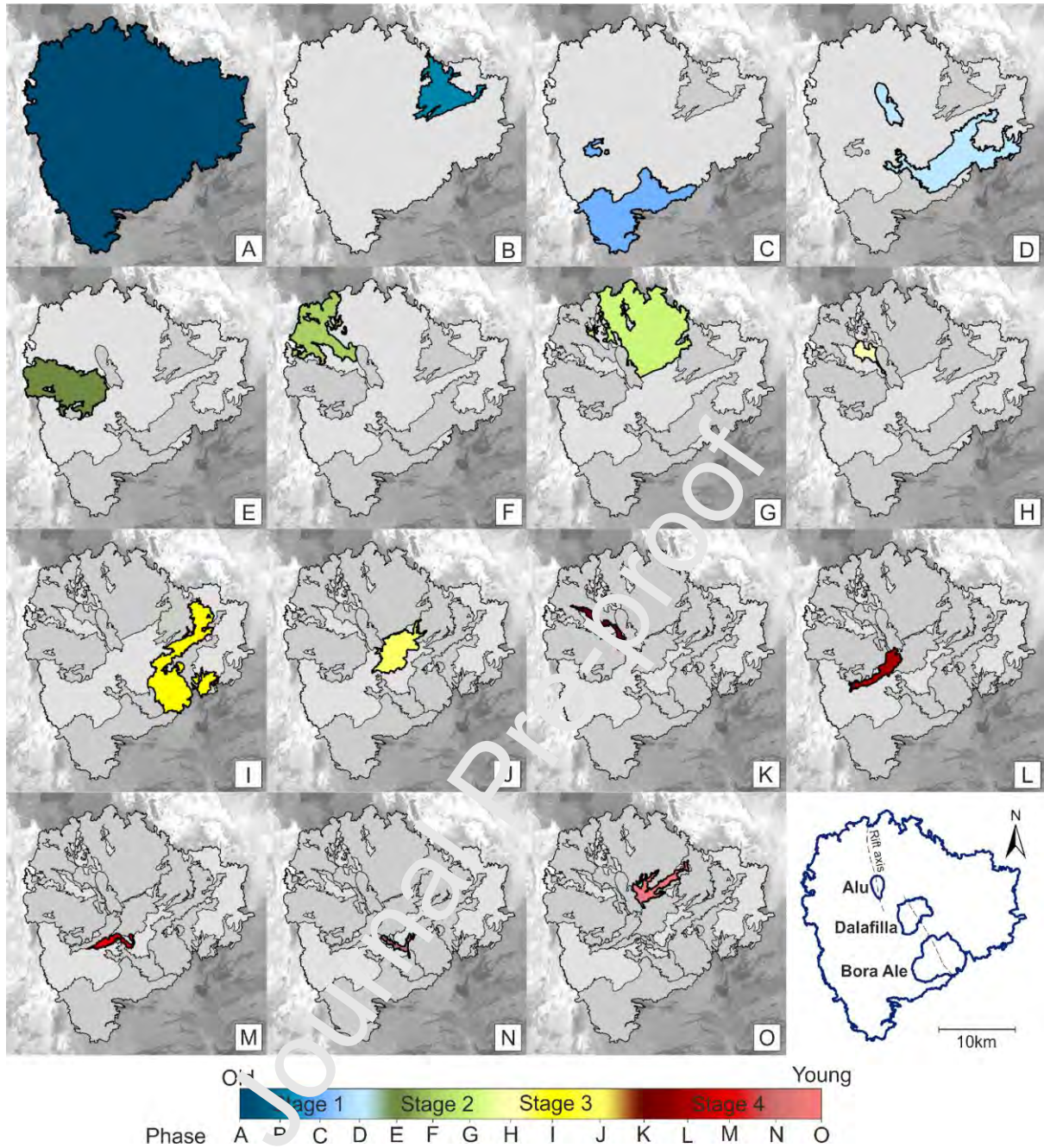
***Figure 3:*** *Chronology of the eruption phases (A-O) across Northern EAVS including Alu, Dalafilla, and Borale, based dominantly on cross-cutting relationships. The phase O is the 2008 eruption. The bottom right panel shows the outline of the area and the location of volcanic centres. The colour bar indicates the relative age of the flow from oldest to youngest (blue to red as in Fig. 2). Stage 1 and 2 (blue and green) show large scale fissure volcanism, followed by stage 3 (yellow) point source volcanism, and stage 4 (red) small volume fissures. Background imagery is Landsat 8 Panchromatic.*

base of the Alu dome (part of Phase D). The total area covered by lava flows within Stage 2 is estimated to be a minimum of 220 km$^2$.

Within this stage of development, the oldest Phase is E, which covered a minimum area of 65 km$^2$ (Figs. 2–3; Table 1). The lava flows were sourced from a fissure to the southwest of the Alu dome and various volcanic cones. These cones occur in two clusters, both NNW oriented, at varying distances from the rift axis (500 m and 3.8 km). The lavas comprise pahoehoe (seen as smooth

surface with flow ridges) and A'a flows (seen as a rubbly surface) that overlap the deposits of Stage 1.

The youngest flows from Phase F onlap the oldest deposits of Phase E, indicating synchronous activity
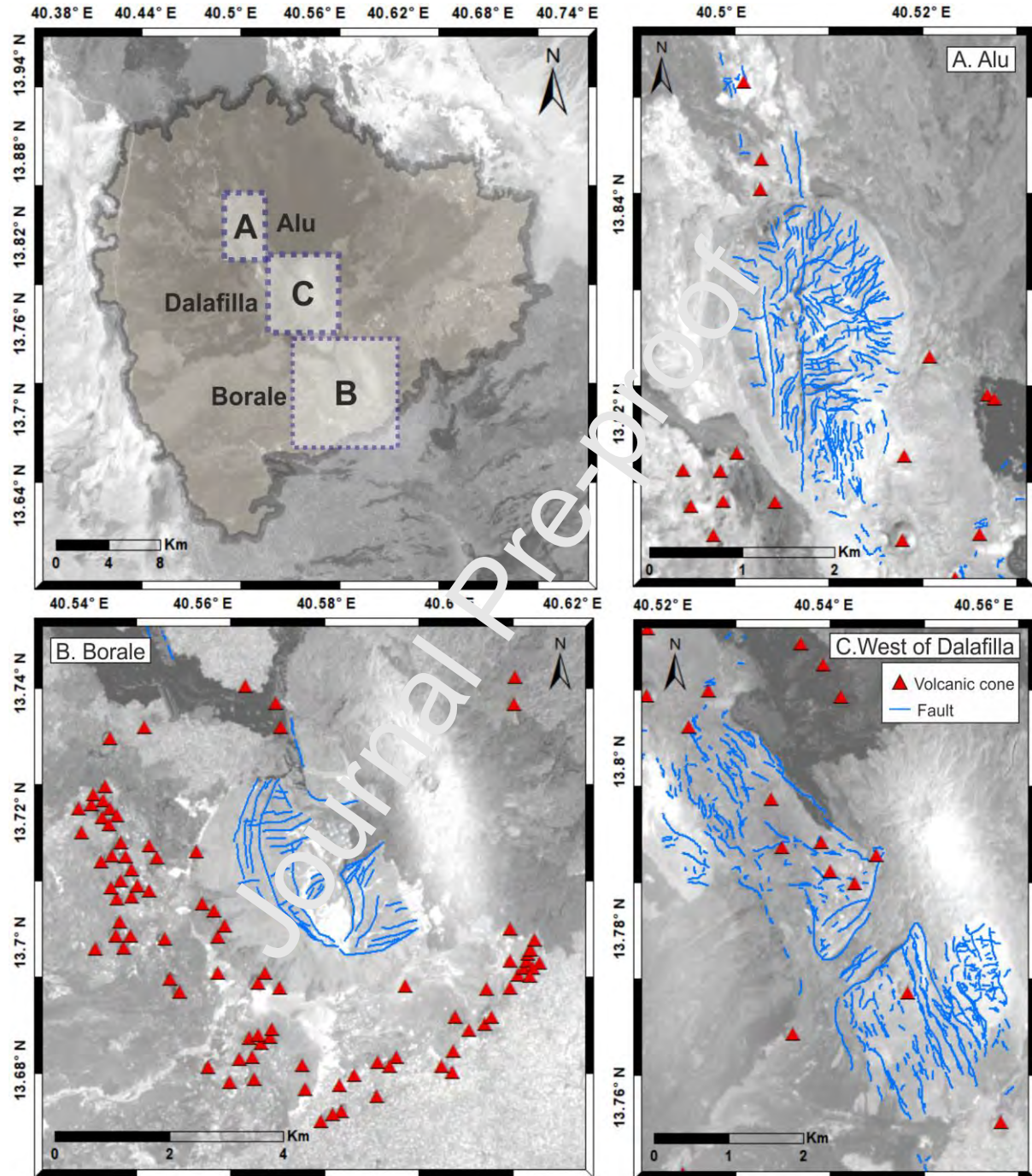


*Figure 4: Map showing the distribution of faults (blue lines) and volcanic cones (red triangles). Map illustrating the locations of the three images (A-C). (A): Alu dome. Orthogonal faults occurring on the Alu dome with volcanic cones and faults expanding radially from the dome. (B): Borale shield and surrounding area. Large curvilinear faults on Borale Shield with an arc-like structure of volcanic cones surrounding the SW side. (C): West of the Dalafilla volcanic edifice where a graben structure can be seen. Background imagery is Landsat 8 Panchromatic.*
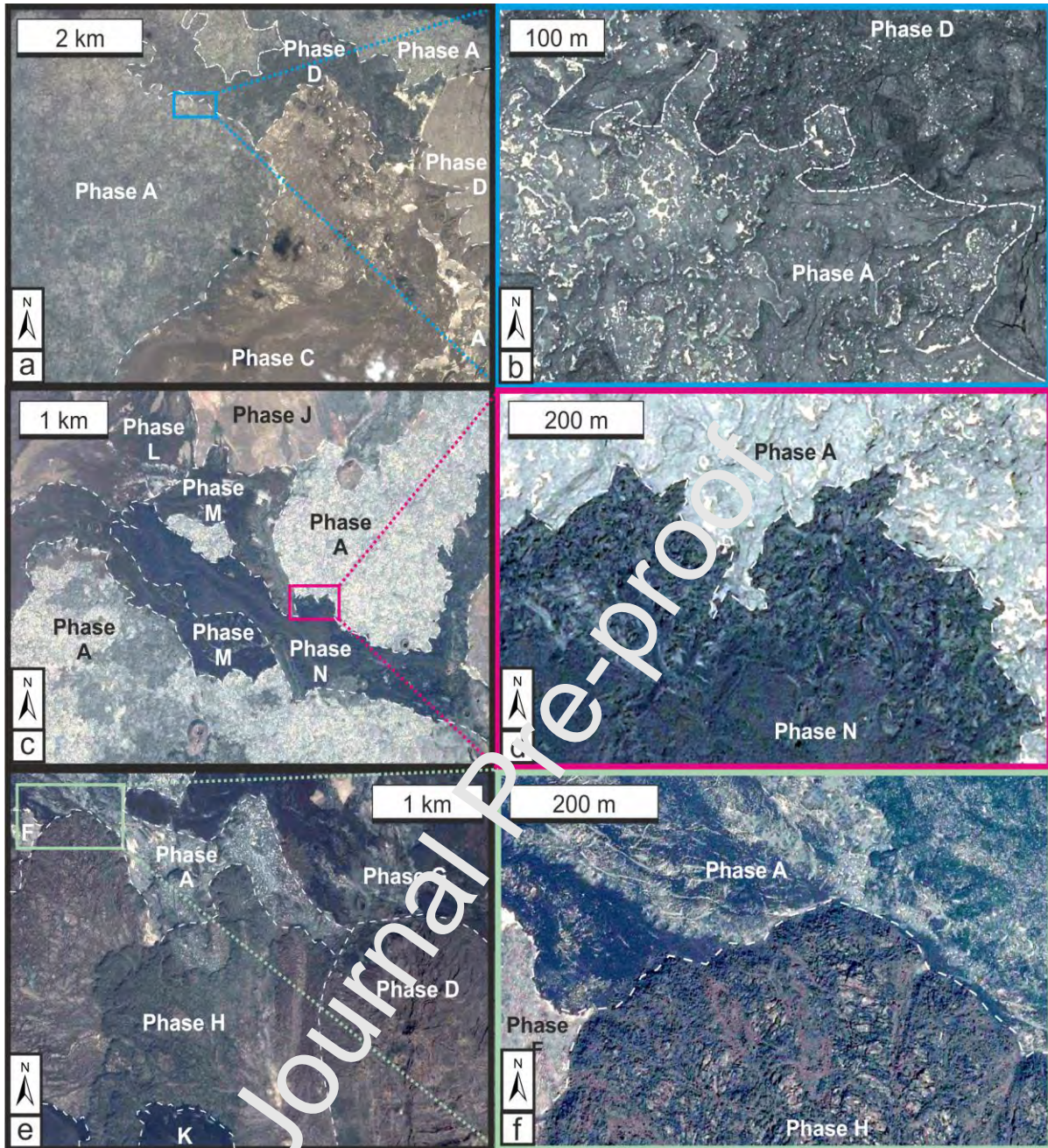
*Figure 5: Various textures of lava flows observed within the Alu-Dalafilla and Borale area. All images are from Google Earth. (a) and (b) illustrate the extensive weathering visible within Phases A-D and increased sediment coverage. (c) and (d) show the Pahoehoe textures visible on the edge of a flow within Phase N. (e) and (f) show the A'a rough texture visible on a flow from Phase H.*

but we note the lack of constraints here on the relative chronology. Phase F occurred on the northwest side of the Alu dome (Fig. 2). Similarly to Phase E, small flows within Phase F were sourced from scoria cones, but the source location of the main flow is obscured by overlying Phase H. The dominant lava type in Phase F is pahoehoe, covering a minimum area of 45.1 km$^2$ (Figs, 2–3; Table 1). The final phase (G) was the largest of Stage 2 covering an area of approximately 110.9 km$^2$ (Figs. 2–3; Table 1). These flows were sourced primarily from fissures on the eastern side of the Alu dome.

### 4.1.1. Stage 3: Alu-Dalafilla and Borale edifices

Stage 3 consists of eruptive phases that occurred at all three volcanic centres. The relative ages of each eruptive phase are unknown due to the lack of overlap and apparent similar degree of weathering. Phase H is the northernmost phase, consisting of two thick A'a lava flows (Fig. 5e, f) produced from a fissure on the northwestern side, and covering a minimum area of 7.6 km$^2$ (Figs. 2–3; Table 1).

Dalafilla (Phase J) comprises at least five lava flows, covering a total of 28 km$^2$. The area is highly faulted with a graben-like structure formed through the centre (Fig. 4c); the faults terminate abruptly at the edge of this structure. Borale (Phase I) comprises a range of volcanic products including pumice and lava flows, which collectively cover a total area of 68.9 km$^2$ (Figs. 2–3; Table 1). The main source of the volcanism in the area is likely the Borale crater but could also include small fissures (about 500 m length) approximately 5 km to the east of the Borale crater.

### 4.1.2. Stage 4: Rejuvenated fissures around Alu-Dalafilla

The fourth stage comprises five phases, each representing a new fissure opening with all deposits being apparently "fresh" but of unknown age. The oldest phase within Stage 4 is Phase K, which produced a lava flow on the southwest of the Alu cone. This lava split into two pahoehoe flows covering a total area of 7.2 km$^2$ (Figs. 2–3; Table 1). This was followed by a fissure opening (Phase L, Figs. 2–3) ~1.4 km in length on the northwest side of Dalafilla, which caused the growth of numerous volcanic cones, approximately 500 m from Alu (Fig. 4).

Phase M consists of three pahoehoe flows sourced from fissures each less than 300 m to the south of Dalafilla, covering an area of 5.8 km$^2$ (Figs. 2–3; Table 1). This was followed by an opening of a fissure (Phase N) > 1.5 km in length on the northwest of Borale, producing a relatively small pahoehoe flow (4 km$^2$; Figs. 5c, d). Finally, on 3 February 2008, two northwest trending fissures one being 2.7 km (Venzke, Sennert & Wunderman., 2009; Pagli et al., 2012) opened on the eastern side of Alu (Phase O) producing four main streams of basaltic lava covering an area of 14.9 km$^2$ (Figs. 2–3; Table 1). ASTER images taken on the 8th November 2008 indicated the presence of a multi-lobed lava field of 9.3 km
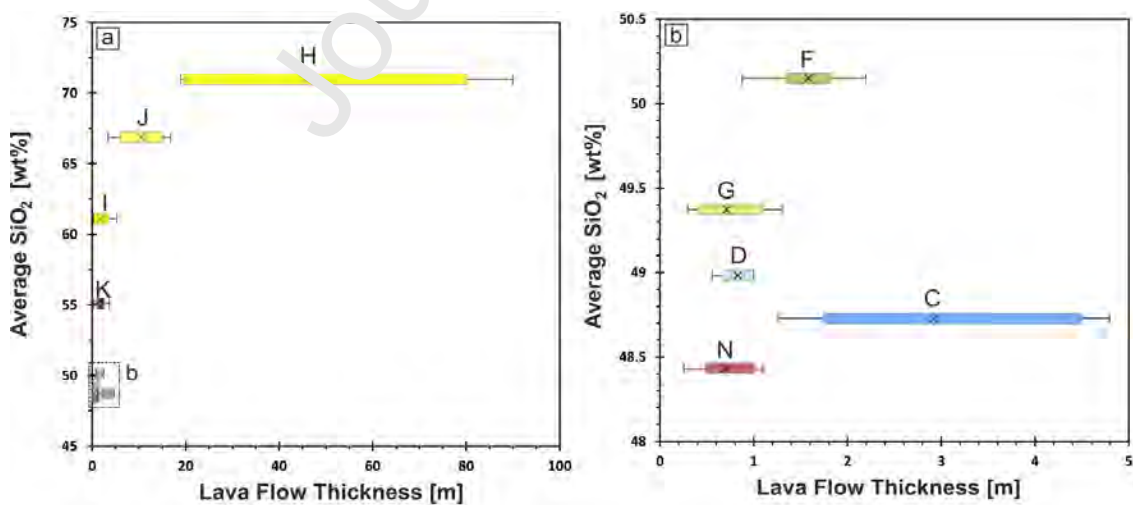


**Figure 6: (a)** *Box and whisker diagram illustrating the variation of lava flow thicknesses with SiO$_2$ content.* **(b)** *Close up of the dotted box shown in (a). Lava flow thickness can be seen to increase with increasing SiO$_2$, except*

*for Phase C. Colours correspond to the Phase as shown in figure 2 and 3. For clarity the letter of the phase is shown above in capital letters.*

| Stage | Phase | Average SiO$_2$ (wt%) | Area (km$^2$) Exposed | Thickness (m) Estimated (average) | Volume (km$^3$) Measured | Min | Max |
|---|---|---|---|---|---|---|---|
| 1 | A | 49.33 | 218.8 | ---------- | ---------- | ----- | ----- |
| | B | *Basalt* | 27.8 | 0.92 | **0.026** | 0.003 | 0.010 |
| | C | 48.73 | 80.1 | 2.92 | **0.234** | 0.101 | 0.385 |
| | D | 48.98 | 53.6 | 0.83 | **0.045** | 0.031 | 0.053 |
| 2 | E | *Basalt* | 65.0 | 1.22 | **0.080** | 0.034 | 0.141 |
| | F | 50.15 | 45.1 | 1.59 | **0.072** | 0.039 | 0.100 |
| | G | 49.37 | 110.9 | 0.72 | **0.079** | 0.036 | 0.142 |
| 3 | H | 70.96 | 7.6 | 45.95 | **0.347** | 0.144 | 0.682 |
| | I | 61.10 | 68.9 | 1.93 | **0.133** | 0.029 | 0.356 |
| | J | 66.89 | 27.8 | 10.62 | **0.295** | 0.096 | 0.425 |
| 4 | K | 55.11 | 7.2 | 1.80 | **0.01** | 0.003 | 0.027 |
| | L | *Basalt* | 12.1 | 1.07 | **0.** | 0.006 | 0.028 |
| | M | *Basalt* | 5.6 | 0.77 | **0.004** | 0.003 | 0.006 |
| | N | 48.43 | 4.1 | 0.69 | **0.003** | 0.001 | 0.005 |
| | O | *Basalt* | 14.6 | 0.90 | **0.013** | 0.007 | 0.026 |

**Table 1:** *Morphometric analysis for each eruptive phase. 'Basalt' is written in the SiO$_2$ column to represent the lack of analyses but estimated composition (48-52 wt% SiO$_2$).*

length that covered an area of 14.9 km$^2$ (Venzke et al., 2009), in agreement with our estimate. Pagli et al. (2012) used satellite images and seismicity to deduce that the eruptive activity peaked after a few hours and then exponentially decreased until stopping on the 6$^{th}$ November 2008.

## 4.2 MORPHOMETRIC ANALYSES OF LAVA FLOWS

The spatial extent of lava flows, as well as their volume and geometry were characterised using morphometric analysis for each of the eruptive phases (Table 1). Lava flow thickness increases with SiO$_2$ from ~0.7 m (49 wt% SiO$_2$) to ~46 m (71 wt% SiO$_2$) with the exception of Phase C (~3 m thick, 49 wt% SiO$_2$, Fig. 6). Across the study area, the most abundant flow type is pahoehoe, with all of the phases within Stage 2 and 4 exhibiting associated features that include smooth and ropey surfaces, and long narrow flows. A'a flows tend to dominate during Stage 3 (H, J) which comprises more felsic lavas and is characterised by thicker flows (10-46 m). These A'a flows are characteristically wide and fan-like, widening (typically from ~1 km to ~2.5 km) towards the flow front. Phase I (Stage 3) contains a mixture of pahoehoe and A'a flows however no A'a flows could be measured for thickness due to overlapping flows and terrain, so the thickness measurements were taken from pahoehoe flows.

Our samples (D137, D138, D140, D143, D147) were collected from the A'a flows at Borale and hence their composition does not represent that of the pahoehoe flows, and no comparison could be made between the thickness and composition of Phase I. While the flows of Phases B, E, L, M, O have not been sampled and hence we have no compositional information; we propose that they are likely to be basaltic in composition based on their low thicknesses (i.e., 0.75 -1.2 m).

Areas covered for each eruptive phase range from 4 to 110 km$^2$ (Table 1) for lava flow stages (Stages 2-4) and a minimum of 37 km$^2$ for the rift floor basaltic phases (Stage 1). The volumes for each eruptive phase (not including A) are less than 0.5 km$^3$, with the basaltic phases (C, D, F, G, N) exhibiting the lowest volumes (0.003 – 0.234 km$^3$; Table 1). The Alu dome, Dalafilla and Borale

stratovolcano, which sourced flows of Stage 3 (H, J), have the greatest volumes with the A'a flows ranging between 0.30 – 0.35 km$^3$. Within Stage 1 and 2, the phases were similar volume to one another yet different to Stage 3; for example Stage 2 erupted low volumes in comparison to Stage 3, but the range was small and tightly defined (0.072-0.08 km$^3$, see Table 1).

### 4.3 LAVA PETROGRAPHY

Lavas from the northern part of the EAVS are variably vesicular (0–48.5%) and porphyritic (0–38%), with 27 of the 30 samples having holocrystalline matrix textures (Supplementary Data SD1, Supplementary Figure SF2). Samples from phases H and J have low vesicularity (<1%) in comparison to the other phases. The basaltic trachy-andesite and basaltic andesite products contains almost no phenocrysts (<1.2%). The phenocryst assemblage of the basaltic products is dominated by plagioclase (0–33.6%, average 13.7%) with subordinate clinopyroxene (0–4.2%, average 1.3%), orthopyroxene (0–5.1%, average 1.1%), and olivine (0-4%, average 0.8%). The phenocryst assemblage of the trachyandesite products is dominated by plagioclase (8.6–22.2%, average 17.4%) and subordinate clinopyroxene (1.2–2.4%, average 2%). Trachyte products contain phenocrysts of plagioclase (11.2–20.6%, average 16%), clinopyroxene (1.4–3.9%, average 2.6%) orthopyroxene (0–1%, average 0.6%) and olivine (0–0.8%, average 0.5%). The phenocryst assemblage of the rhyolite is dominated by plagioclase (4.6%) with small amounts of orthopyroxene and clinopyroxene (<0.4%). The groundmass consists of microlites of similar mineralogy to the phenocrysts. Accessory minerals within the groundmass include magnetite and apatite. Selected samples from Stage 3 (D141) and Stage 4 (CH23, F55) do not contain any discernible phenocrysts.

A variety of textures (Fig. 7) are observed amongst the macro (here defined as >1 mm) plagioclase crystals within samples D156, F59 and CH20 (Stages 1 and 3). Using the classification of plagioclase textures from Bennett et al. (2019), all the macro plagioclase phenocrysts can be described as tabular (sub- to euhedral) containing elongate and amoeboid melt inclusions mostly parallel to the twinning planes (Fig. 7a). Resorption textures were observed in most plagioclase phenocrysts, with internal resorption (defined as dissolution surface inside the phenocryst) being the most common. However, several plagioclases (D156) show both internal and external resorption (Fig. 7b). Some plagioclase phenocrysts exhibit simple and oscillatory zoning (Fig. 7b), the former being more common.
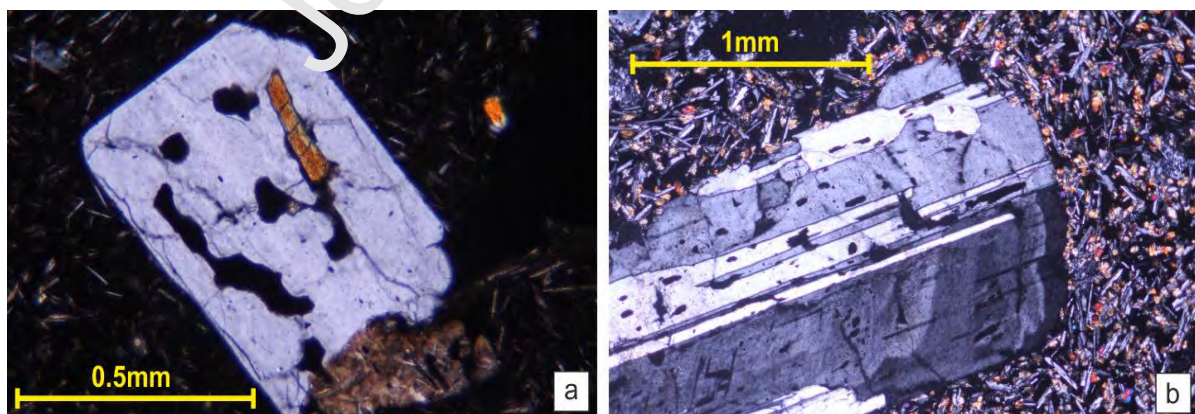


**Figure 7:** Plagioclase phenocryst textures. (a) Left: Plagioclase crystal from sample F59 (Phase J, 13.7947N 40.54509E) showing a pyroxene crystal partially enclosed within an amoeboid glass inclusion (sieve texture). (b) Right: Plagioclase crystal in sample D156 (Phase D, 13.70686N 40.572685E) highlighting the thick oscillatory zoning and dissolution rims with some melt inclusions in the centre

### 4.4 LAVA GEOCHEMISTRY

The results of major element XRF analyses are presented in Table 2. The majority of samples (>60%) are classified as basalts (Table 2; Fig. 8), with the remainder of the samples being basaltic trachy-andesite, trachy-andesite, trachyte or rhyolite in composition. All samples are tholeiitic (i.e., they lie just below the tholeiitic/alkaline boundary, see Fig. 8) but have a moderate alkaline affinity (illustrated by the samples being in the transitional zone on the TAS diagram). The total alkali values range between 3.1 and 8.8 wt%, with corresponding $SiO_2$ values of 48 to 71 wt% (Fig. 8). All of the samples from Stages 1 and 2 are basaltic (Fig. 8) with $SiO_2$ content being tightly defined (48.0–50.5 wt%). They are characterised by MgO contents of 4.8–7.8 wt%, $TiO_2$ of 2–3 wt% and $Al_2O_3$ of 13.5–17 wt% (Fig. 9). In contrast, Stage 3 spans a wide range of compositions from basaltic trachy-andesite to rhyolite (56–71 wt% $SiO_2$), with lower values of MgO (0.4–2.6 wt%), $TiO_2$ (0.5–2.1 wt%) and $Al_2O_3$ (12.3–14.6 wt%) as seen in figure 9. Within Stage 4, a relatively wide distribution of compositions is observed, with samples from Phase K being basaltic andesite (53-55 wt% $SiO_2$) and Phase N being basaltic (48 wt% $SiO_2$; Fig. 8).

The variation of major elements versus MgO are shown in figure 9. $SiO_2$, $K_2O$ and $Na_2O$ exhibit a well-defined increase with decreasing MgO, with an inflection point at approximately 4 wt% MgO. $Al_2O_3$ and CaO appear to consistently decrease as MgO decreases (Fig. 9), forming a positive linear trend, although there are some outliers ($Al_2O_3$) to this trend (D157, M7, Stage 1; D149, D150, D155, Stage 4).
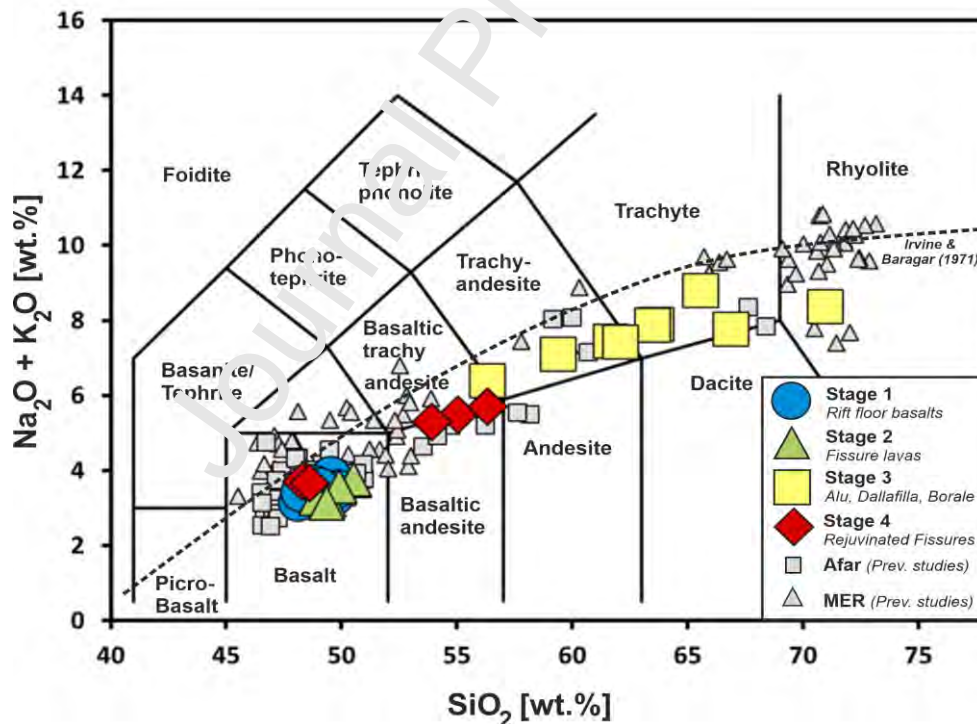


**Figure 8**: *Total Alkali-Silica diagram after LeBas et al. (1986) showing the whole rock (WR) compositions from the samples across the north of EAVS. Samples from the four stages identified in the chronology are shown by* larger symbols: *1 = blue* circle*, 2 = green* triangle*, 3 = yellow* square*, 4 = red* diamond. Small grey s*quares show whole rock compositions from across Afar (Barrat et al 1998; Ferguson et al., 2013;; Hagos et al., 2016). Small grey triangles show whole rock data from across the MER (Peccerillo et al., 2003; Hutchison et al., 2016; Feyissa et al., 2017). Dashed line shows the division of volcanic rocks into alkaline (above) and subalkaline/tholeiitic (below) after Irvine and Baragar (1971).*

| Sample | D152 | G43 | G66 | G65 | D156 | M6 | M7 | D15 |
|---|---|---|---|---|---|---|---|---|
| Sample type | Lava | Lava | Lava | Lava | Lava | Lava | Lava | Lava |
| Longitude | 40.569416 | 40.420101 | 40.448575 | 40.466646 | 40.572685 | 40.552593 | 40.556159 | 40.51044 |
| Latitude | 13.729510 | 13.838550 | 13.681500 | 13.654390 | 13.706860 | 13.726270 | 13.725080 | 13.83839 |
| $SiO_2$ | 49.34 | 49.12 | 49.53 | 48.74 | 49.67 | 48.10 | 48.20 | 49.87 |
| $Al_2O_3$ | 13.65 | 13.87 | 14.05 | 14.99 | 16.91 | 14.81 | 16.76 | 14.02 |
| $Fe_2O_3$ | 14.04 | 13.65 | 13.10 | 12.86 | 11.75 | 12.23 | 11.30 | 12.91 |
| CaO | 10.57 | 10.35 | 10.42 | 10.45 | 11.31 | 10.96 | 11.94 | 11.00 |
| MgO | 5.65 | 5.82 | 5.71 | 7.15 | 4.81 | 7.82 | 6.00 | 6.31 |
| $Na_2O$ | 2.95 | 3.01 | 3.22 | 3.02 | 2.77 | 2.60 | 2.78 | 2.96 |
| $K_2O$ | 0.62 | 0.64 | 0.66 | 0.63 | 0.52 | 0.54 | 0.62 | 0.56 |
| $TiO_2$ | 2.97 | 2.81 | 2.83 | 2.56 | 2.28 | 2.55 | 2.55 | 2.37 |
| MnO | 0.20 | 0.20 | 0.19 | 0.18 | 0.17 | 0.17 | 0.17 | 0.19 |
| $P_2O5$ | 0.42 | 0.42 | 0.42 | 0.3 | 0.33 | 0.37 | 0.46 | 0.34 |
| $SO_3$ | 0.01 | 0.02 | 0.01 | 0.0 | 0.01 | <0.01 | 0.01 | <0.01 |
| LOI | -0.62 | -0.41 | -0.15 | -0.62 | -0.22 | -0.31 | -0.47 | -0.55 |
| Total | 99.80 | 99.50 | 99.99 | 100.36 | 100.31 | 99.84 | 100.32 | 99.98 |
| Rock type | Basalt | Basalt | Basalt | Basalt | Basalt | Basalt | Basalt | Basalt |
| Stage | 1 | 1 | 1 | 1 | 1 | 1 | 1 | 1 |
| Phase | A | A | A | C | D | D | D | D |

**Table 2:** XRF major element data for all 30 samples analysed. See figure 2 for sample locations. Location information is also provided in decimal degrees (longitude and latitude are degrees east and north, respectively). All concentrations are reported as wt%. Rock types are allocated based on the Total Alkali-Silica classification diagram (Fig. 8). Errors associated with the XRF measurements are given in Supplementary data (SD1).

| Sample | F49 | D2 | D7 | D8 | D141 | CH20 | D137 | D13 |
|---|---|---|---|---|---|---|---|---|
| Sample type | Lava | Lava | Lava | Lava | Pumice | Lava | Lava | Lava |
| Longitude | 40.465840 | 40.529498 | 40.540674 | 40.558864 | 40.593194 | 40.482635 | 40.617804 | 40.620 |
| Latitude | 13.903860 | 13.925020 | 13.908740 | 13.921460 | 13.700500 | 13.838780 | 13.713340 | 13.707 |
| $SiO_2$ | 49.41 | 48.90 | 49.88 | 49.33 | 65.55 | 70.96 | 63.63 | 61.6 |
| $Al_2O_3$ | 14.15 | 13.94 | 13.56 | 14.15 | 12.78 | 12.73 | 12.63 | 12.7 |
| $Fe_2O_3$ | 12.33 | 12.19 | 14.58 | 12.04 | 4.89 | 4.18 | 9.56 | 10.4 |
| CaO | 11.63 | 11.94 | 9.88 | 11.89 | 2.03 | 1.44 | 2.98 | 3.6 |
| MgO | 6.57 | 6.50 | 5.46 | 6.72 | 0.61 | 0.43 | 0.97 | 1.4 |
| $Na_2O$ | 2.73 | 2.75 | 3.00 | 2.62 | 6.22 | 5.68 | 5.31 | 5.09 |
| $K_2O$ | 0.50 | 0.50 | 0.58 | 0.50 | 2.57 | 2.69 | 2.59 | 2.3 |

| | | | | | | | | |
|---|---|---|---|---|---|---|---|---|
| TiO$_2$ | 2.19 | 2.20 | 2.95 | 2.11 | 0.53 | 0.55 | 1.35 | 1.6? |
| MnO | 0.18 | 0.18 | 0.22 | 0.18 | 0.15 | 0.15 | 0.23 | 0.24 |
| P$_2$O$_5$ | 0.31 | 0.31 | 0.52 | 0.31 | 0.09 | 0.07 | 0.36 | 0.5? |
| SO$_3$ | 0.15 | 0.68 | 0.07 | 0.27 | 0.07 | <0.01 | 0.04 | 0.0? |
| LOI | -0.18 | -0.23 | -0.79 | -0.15 | 4.50 | 0.38 | -0.24 | -0.3? |
| Total | 99.97 | 99.86 | 99.91 | 99.97 | 99.99 | 99.26 | 99.41 | 99.5? |
| Rock type | Basalt | Basalt | Basalt | Basalt | Pumice | Rhyolite | Trachyte | Trachyan... |
| Stage | 2 | 2 | 2 | 2 | 3 | 3 | 3 | 3 |
| Phase | F | G | G | G | I | H | I | I |

Table 2 continued.

| Sample | D147 | D148 | F59 | D1?3 | F54 | F55 | D149 |
|---|---|---|---|---|---|---|---|
| Sample type | Lava | Lava | Lava | Lava | Lava | Lava | Lava |
| Longitude | 40.584277 | 40.580235 | 40.549509 | 40.434757 | 40.500869 | 40.498528 | 40.576490 |
| Latitude | 13.750910 | 13.745200 | 13.79?700 | 13.846130 | 13.813780 | 13.817850 | 13.751270 |
| SiO$_2$ | 56.33 | 59.38 | ?6.?9 | 55.06 | 53.92 | 56.34 | 48.41 |
| Al$_2$O$_3$ | 14.32 | 12.89 | 12.88 | 13.33 | 13.28 | 13.52 | 16.31 |
| Fe$_2$O$_3$ | 11.39 | 10.96 | 7.05 | 12.89 | 13.04 | 11.97 | 11.70 |
| CaO | 5.82 | 4.?3 | 2.52 | 7.00 | 7.12 | 6.39 | 11.28 |
| MgO | 2.55 | ?.9? | 0.81 | 3.57 | 3.62 | 2.98 | 5.77 |
| Na$_2$O | 4.97 | 5.1? | 5.45 | 4.60 | 4.44 | 4.60 | 3.01 |
| K$_2$O | 1.42 | 1.96 | 2.31 | 0.88 | 0.85 | 1.10 | 0.73 |
| TiO$_2$ | 2.02 | 1.99 | 0.95 | 2.78 | 2.82 | 2.38 | 2.66 |
| MnO | 0.25 | 0.27 | 0.19 | 0.21 | 0.21 | 0.22 | 0.18 |
| P$_2$O$_5$ | 0.8? | 0.73 | 0.21 | 0.68 | 0.66 | 0.78 | 0.54 |
| SO$_3$ | 0.02 | 0.06 | 0.01 | 0.01 | 0.06 | 0.01 | 0.01 |
| LOI | -0.27 | -0.09 | 0.24 | -0.57 | -0.37 | -0.44 | -0.64 |
| Total | 99.63 | 99.55 | 99.51 | 100.44 | 99.65 | 99.84 | 99.96 |
| Rock type | Basaltic trachyandesite | Trachyandesite | Trachyte | Basaltic andesite | Basaltic andesite | Basaltic andesite | Basalt |
| Stage | 3 | 3 | 3 | 4 | 4 | 4 | 4 |
| Phase | I | I | J | K | K | K | N |

Table 2 continued

P$_2$O$_5$, Fe$_2$O$_3$(t) and TiO$_2$ all show a steep positive trend between 0–4 wt% MgO, and then level off to an almost horizontal trend at MgO values > 4 wt% (Fig. 9).

Stage 1 and 2 are clustered with similar values across all major elements (Fig. 9). Stage 3 shows a greater range in abundance for all major elements, producing clear trends. Phase N (Stage 4) lavas are similar in composition to the basalts of Stage 1 and 2 for all major elements except $Al_2O_3$, in which they are enriched (Fig. 9). The other samples from Stage 4 (Phase K) have major element chemistry that lies between that observed for the basalts (Stages 1 and 2) and Stage 3.

Modelling of the fractionating phases was carried out using two models: (1) rhyolite MELTS (Gualda & Ghiorso, 2015); and (2) a mass balance model which uses the measured compositions of minerals observed from the samples (Fig. 10). Both models' starting composition was that of the most primitive sample (M6; Table 2), and the MELTS model used a $H_2O$ content of 3 wt% and an $fO_2$ of NNO-4 as these were the best fit for the data (see Supplementary Figures SF3 and SF4). The $H_2O$ and $fO_2$ contents are within ranges previously estimated for the Ethiopian region (Gleeson et al., 2017; Field et al., 2013; respectively). The pressure-temperature (P-T) conditions for the MELTS sequence were set to P = 500 to 100 MPa and T = 800 to 1300°C, the accepted values for crustal thickness (Maguire et al., 2006), and lower than the estimated mantle temperature of 1490°C (Rooney, Herzberg & Bastow., 2012). The mass balance model uses mineral compositions from Alu-Dalafilla and Borale: CH20, F53 and G65 (Bizouard et al., 1980). Both models predicted similar assemblages with the dominant phases being olivine, clinopyroxene, plagioclase feldspar, orthopyroxene, apatite and Fe-Ti oxides.

While MELTS employs more intensive parameters as constraints (pressure, temperature and $fO_2$), the calculated liquid line of descent does not fit the observed data, nor the mass balance model (Fig. 10). This could be due to a combination of factors: rhyolite MELTS not being optimised for alkaline systems; the mineral compositions being calculated from phase diagrams rather than to those observed; and the model also predicted an early onset of Rhm oxides (a mixture comprised of hematite, ilmenite, giekelite and pyrophanite) and spinel crystallisation, which causes the $TiO_2$ and $Fe_2O_3$(t) (respectively) values to decrease too rapidly.

# 5   DISCUSSION

## 5.1 COMPOSITIONAL EVOLUTION

Since the apparent onset of volcanism at Alu-Dalafilla and Borale, the magma composition has been dominantly basaltic with intervals of felsic magmatism. Our geochemical modelling (Fig. 10) of Stages 1 and 2 (48-50.5 wt % $SiO_2$) show only early stages of fractional crystallisation and melt evolution with the main crystallising phases being those observed petrographically (i.e., olivine, clinopyroxene, and plagioclase). This observation, alongside the lack of complex textures (i.e., zoning) within phenocrysts that are observed in Stage 3 (Fig. 7), indicate that the magmas have not experienced prolonged storage and were not subject to much variability in the sub-volcanic plumbing system.

Stage 3 represents a step-change from fissure-dominated basaltic volcanism to felsic volcanism at the volcanic centres. There is an increase in abundance and size of plagioclase feldspar phenocrysts within these lavas, with most phenocrysts showing a range of textures including normal and oscillatory zoning, internal resorption surfaces and melt inclusions (Fig. 7). The presence of melt inclusions that are elongate parallel to the twins of the plagioclase feldspar indicates that these are formed as a result of resorption due to twins being formed after crystallisation (Dungan & Rhodes, 1978; Nelson &
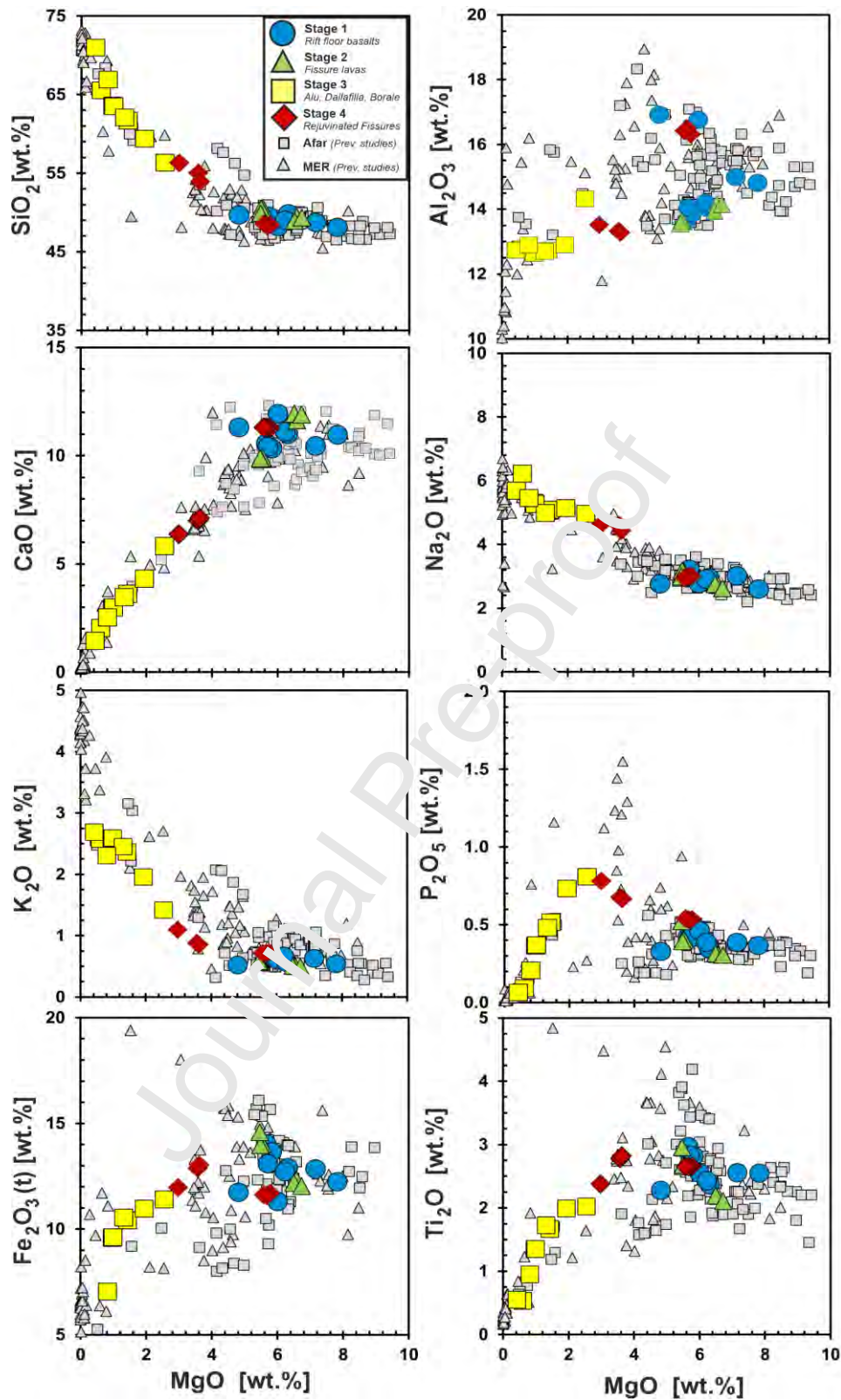
*Figure 9: Major elements binary diagrams showing the whole rock (WR) compositions from the samples across the north of EAVS. Samples from the four stages identified in the chronology are shown by larger symbols: 1 = blue circle, 2 = green triangle, 3 = yellow square, 4 = red diamond. Smaller grey squares show whole rock compositions from across Afar (Barrat et al 1998; Ferguson et al., 2013; Hagos et al., 2016). Small grey triangles show whole rock data from across the MER (Peccerillo et al., 2003; Hutchison et al., 2016; Feyissa et al., 2017).*

Montana, 1992). This observation, in addition to the internal resorption surfaces, indicate that the plagioclase phenocrysts have experienced multiple periods of disequilibrium which could result from: (1) the mixing of a hot basaltic melt from depth with a more evolved magma in a shallow magma storage system (rejuvenation); (2) change(s) in pressure associated with rapid ascent that would change the plagioclase composition that is in equilibrium (Nelson & Montana, 1992).

While the compositions within Stage 4 (K, N) are different (Figs. 8–9), all flows within the stage were sourced from fissures and have very similar physical characteristics (i.e., flow textures) and similar morphometric attributes (Table 1). This, combined with the lack of compositional data from the other three phases (L, M, O), meant that until further data can be collected they have been grouped together based mainly on their physical characteristics.

Both of our models (Fig. 10) indicate that the variation between and within all the stages of volcanism can be explained through fractional crystallisation as the main mechanism for evolution of the magma system. No significant mixing or assimilation of continental crust is required to explain the major element compositions (Fig. 10). However, this does not exclude the possibility of assimilation occurring, as it may only be detectable using trace elements or isotopic compositions (Ayalew et al., 2019). The crust beneath the Danakil depression are amongst the thinnest in Afar at ~15 km (Makris & Ginzburg, 1987), and has a density and P wave velocity consistent with it being continental crust intruded with mafic intrusions (Bastow & Keir, 2011; Ebinger et al., 2017). If the samples experienced fractional crystallisation within a crust containing abundant basaltic intrusions, crustal assimilation may not be easily detectable due to chemical similarities between the magma and intruded crust. The exception to this is the outliers (D156, M7 from Stage 1 and D149, D150, D155 from Stage 4) in Figure 10. The outliers could be a result of plagioclase accumulation (as illustrated in Figure 10), most likely due to density settling occurring within the magmatic system.

On the basis of the lack of assimilation observed within the samples and the spatial distribution of basalts versus trachytes and rhyolites (Figs. 2–10; Table 2), we propose a complex plumbing system of dykes independent of a shallow storage system consisting of stacked sills, beneath each of the volcanic edifices (Alu Dome, Dalafilla and Borale) along the rift axis. The regular replenishment of the sills maintains their temperature while they progressively undergo fractional crystallisation resulting in the evolved lavas of Stage 3 (Fig. 10). Alongside this, magma can ascend rapidly from depth via intrusions with only short periods of stagnation, allowing for very little fractional crystallisation to occur before the magma erupted at fissures on the volcano flanks producing the lava flows associated with Stages 1, 2 and 4 (Fig. 11).

This interpretation of the plumbing system is consistent with both the saucer-shaped sill model proposed by Magee et al. (2017), as well as the evidence for numerous magma storage systems at various depths; e.g., 1 km, 4 km, and 12 km (Pagli et al., 2012; Illsley-Kemp et al., 2018a). Our model is also supported by anisotropy data which shows overall negative anisotropy across the EAVS, indicating dominantly vertical features such as faults and dykes across the region (Kendall et al., 2005; Chambers et al., in prep). However, the low resolution of this data (40 km) could therefore mean that while the melt pathways are dominantly vertical, there can also be a small scale (<10 km length) sill network beneath Alu, Dalafilla and Borale's volcanic edifices, consistent with that modelled from InSAR data, associated with the 2008 eruption (Pagli et al., 2012).
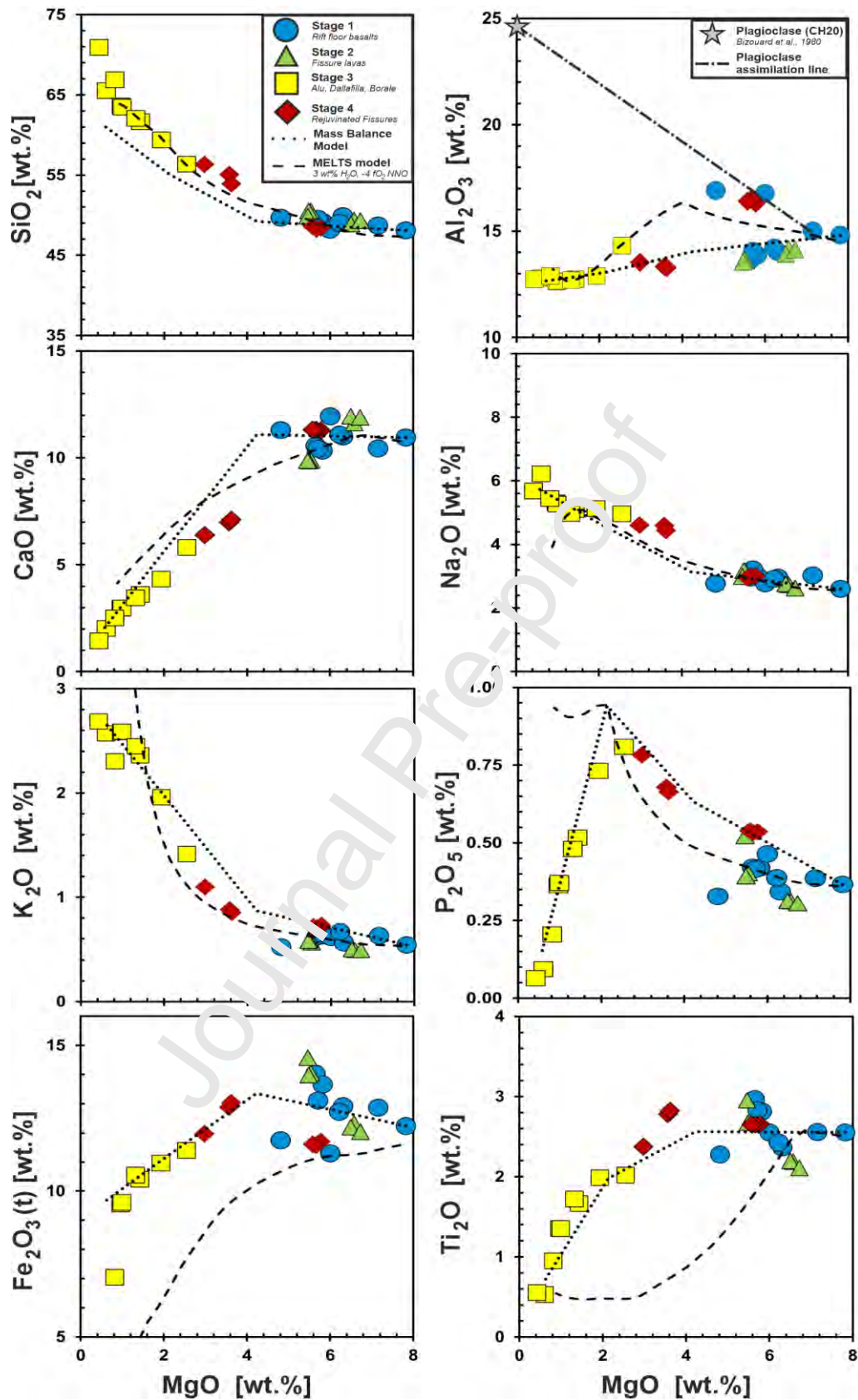
**Figure 10:** *Major elements binary diagrams showing the modelling of the liquid line of descent as the melt evolves. The symbols are as in figure 8 and 9. The dotted line indicates the results of a mass balance model. The dashed line shows the results of Rhyolite Melts v1.2 model at 3wt% $H_2O$, and -4 $fO_2$ (NNO).*

## *5.2 SPATIAL EVOLUTION*

The mode of formation of the Alu dome has been a topic of debate since the 1960's. Whilst Alu was originally interpreted as a shield volcano (Barberi et al., 1970), it has more recently been suggested that it may constitute a dome on the basis of saucer-shaped sill emplacement at depth (Magee et al., 2017). The overlapping relationships documented here would suggest that the dome structure post-dates the flow of Phase H, due to the onlapping of flow H to the steep side of the Alu-dome (Fig. 2, 5e), adding support to the inferred saucer-shaped sill forming the dome (Magee et al., 2017).

Across the area, the spatial distribution of fissures and lavas produce patterns that are unique to each stage. After Phase A, the remainder of Stage 1 is confined to the southern part of the area surrounding Borale. Following this, Stage 2 progresses clockwise around the Alu dome (fissures 2-4, Fig. 11a), with consistent lava volumes across each phase within the stage (Table 1). Similarly, progressive fissure opening occurred within Stage 4. These advancements of fissures occurred in an anticlockwise direction around the Alu dome (Fig. 11). The curvilinear nature of the fissure openings and the presence of volcanic cones perpendicular to these fissures indicates the presence of radial fractures, typically associated with cone sheet complexes (Anderson 1937; Bistacchi et al., 2012). It is therefore considered likely that the cause of the systematic opening of the fissures within the Alu-Dalafilla region is the formation of a cone sheet sourced from sills beneath the Alu dome (Fig. 11b), related to excess stresses associated with uplift (Anderson, 1937).

Based on the overlapping relationship of Phase H (sourced from fissure 5; Fig. 11) with the Alu dome, it is known that the opening of fissures 1-5 predates the uplift that produced the Alu dome currently observed. In order to form the fissures and associated cone sheet before the doming event, there must have been repeated uplift and subsidence linked to sill emplacement beneath Alu. Alongside this, the repeated uplift and subsidence could cause variations in the stress fields of the region, resulting in shifting of the locations of the fissure opening to where the stress is greatest. This could explain the observed variability in the location of fissures within stage 2 (fissures 2-4, Fig. 11), as the dykes feeding the fissures could then exploit the pathways created by such a cone sheet.

At Borale, there are numerous curvilinear faults and a series of scoria cones that form an arc shape around Borale's volcanic centre (Figs. 4b, 11a), suggesting the presence of ring faults and ring dykes (respectively; Fig. 11c) with the ring dykes providing a melt pathway for the scoria cones. The presence of these features is likely due to the subsidence of a previous volcanic centre at Borale (Anderson 1937; Kresten, 1980; Fig. 11). The scoria cones overlie, and hence post-date the surrounding lava flows of phases A-D (Fig. 2). Further field analysis and radiometric dating is required to better constrain the timing of volcanic activity associated with the ring dyke emplacement. It must also be noted that there is a chance of scoria cones in the area which have been eroded or buried under lava flows that postdate cone emplacement.

The chronology of the lava flows within the region indicate the relative timings of fissure eruptions that are shown in Figure 11a. Due to the overlap relationships between lavas of Phase E and F, discussed in section 4.1.2, there is some uncertainty around the relative timing of opening of the fissures associated with the two phases (E and F, Fig. 11a).
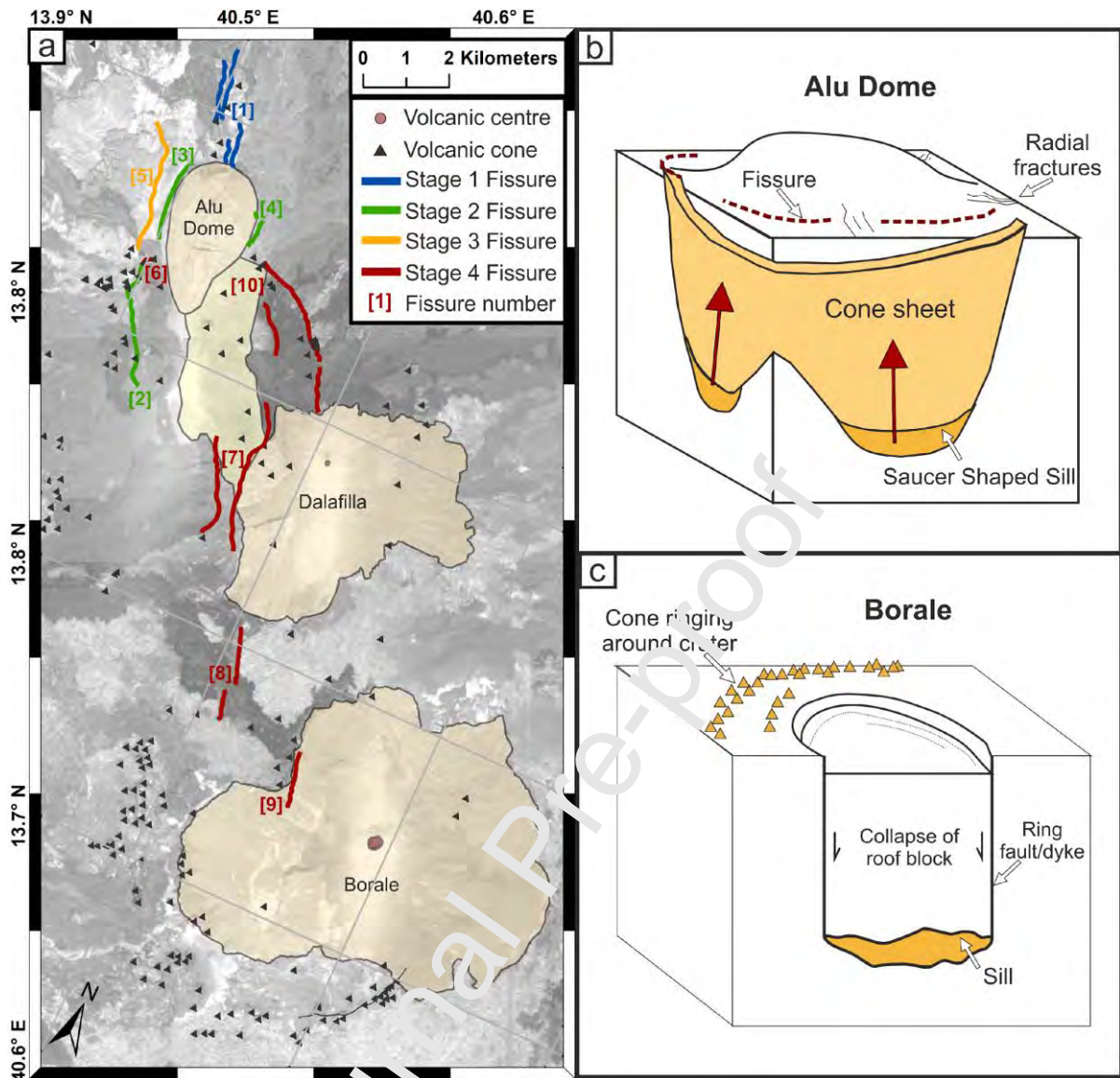
**Figure 11: (a)** Left: Annotated map illustrating the systematic progression of the fissures around the Alu-Dalafilla and Borale area. The numbers shown are the fissures in chronological order. Background imagery is Landsat 8 Panchromatic. **(b)** Top right: Schematic diagram showing the growth of cone sheets beneath the Alu dome. **(c)** Bottom right: Schematic diagram of ring dykes and volcanic cones forming around Borale. (b) and (c) are based on the theory by Anderson (1937).

The presence of ring dykes and cone sheets supports the concept of a shallow storage system consisting of stacked sills beneath the volcanic edifices of Alu and Borale. On the basis of the timing of Stage 2 fissures, Phase H and the Alu dome uplift, we propose that Alu has experienced numerous phases of uplift and subsidence. Initial uplift of the Alu dome could have created a cone sheet which was interacted and exploited by off- axis dykes during the fissure events of Stage 2. Following this, Phase H (Stage 3; Fig. 2) could have been sourced from the shallow sill that lies directly beneath Alu and was transported via the cone sheet to erupt at fissure 5 (Fig. 11a). Subsequent uplift of Alu may have occurred post Phase H, due to re-filling of the saucer shaped sill beneath the edifice, producing the present-day Alu dome.

## 5.3 RELEVANCE TO RIFT EVOLUTION

The volcanic segments in Afar are the current locus of extension and volcanism in the rift (Hayward & Ebinger, 1996). They have a similar length, width, spacing, and surface morphology to the second order magmatic segments of mid-ocean ridges (Schouten, Dick & Klitgord., 1987; Ferguson et al., 2013; Carbotte et al., 2016). Most of the volcanic segments in Afar (Fig. 1b) are ~70-km-long, 20-km-wide, and have a surface morphology characterised by a segment centred axial volcanic high, transitioning to a fault bound axial graben towards the segment tips (e.g., Keir et al., 2009), similar to the segment morphology at slow spreading ridges. The similarity in segment morphology is potentially linked to the extension rate of Afar (~15-20 mm/yr), being at the slow end of that of slow spreading ridges (Jokat et al., 2003). The less mature MER also has magmatic segments of similar size and morphology to Afar (e.g., Ebinger & Casey, 2001; Siegburg et al., 2020) but rifting is at a slower rate (4.5 mm/yr, Bilham et al., 1999).

In contrast to most of Afar and the MER, the surface morphology at the EAVS is dominated by a segment long axial high, with a distinct lack of an axial graben except at the distal tips of the volcanic segment (Keir., 2014). The distinctive axial high, along with the geodetic evidence for shallow axial sills, has been used to propose that the plumbing system is more akin to that of spreading ridges where elevated magma supply and flux occurs in a similar manner to that observed at most fast spreading ridges; e.g., the East Pacific Rise (Pagli et al., 2012).

In support of this hypothesis, the petrology and geochemistry of the EAVS described here shares particular affinities to ocean ridges characterised by elevated melt flux, such as, for example, the Galapagos Spreading Centre (GSC). Basalts from both the EAVS and GSC are dominantly Fe-Ti basalts ($FeO_t$> 12 wt %, $TiO_2$>2 wt %, Colman et al., 2012). Colman et al. (2012) shows the compositional variation at high magma supply regions of the GSC (average MgO = 5.89 wt %, range 4.66) is much larger than that observed at low magma supply regions of the GSC (average MgO = 7.93 wt%, range 0.86). The EAVS basalts (average MgO = 6.04 wt %, range 3.01, Fig. 9, 10) are similar to those of the high magma supply regions of the GSC, supporting the hypothesis that the EAVS is similarly a region of elevated melt flux.

While the EAVS draws many parallels to a mid ocean ridges with elevated melt flux, the EAVS also shares geochemical characteristics with magmatic segments within less evolved rift zones; i.e., the MER. The volcanic products of the segments within MER have a basalt-to-rhyolite compositional range (43-76 wt % $SiO_2$, Hutchison et al., 2018) similar, although larger, to that observed in the EAVS (48.5–70 wt % $SiO_2$, Fig. 8). Basaltic products, across both the MER and EAVS, are dominantly transitional with some tholeiitic samples at the EAVS (Supplementary data SD1). Silicic products of the MER (with the exception of Gedemsa, Hutchison et al., 2018) are strongly peralkaline (molar $Na_2O + K_2O/Al_2O_3$ >1, Hutchison et al., 2018), yet the silicic products of the EAVS are only mildly peralkaline. While the proportion of silicic products is much higher in the MER compared to that of the EAVS, when modelled, some products of the MER show that fractional crystallisation is the dominant factor controlling compositional variations (Rooney et al 2007), comparable to our EAVS samples. This, alongside the similarity of the major element abundances between the EAVS and some magmatic segments of the MER, indicates they may share similar origins but other indicators (i.e., trace elements and isotopic evidence) would be needed to confirm. However, the higher abundance of basaltic products in the EAVS supports the hypothesis that the area is further along in its evolution to becoming a mid ocean ridge (Wolfenden et al., 2004; Corti, 2009).

Rift morphology, plumbing system style, and geochemical attributes supports the interpretation of the EAVS being a basalt-rich volcanic segment with anomalously elevated melt supply within a magmatic rift at the point of breakup. The rift floor of the Danakil depression is below sea level and results in interbedded lava flows and evaporites, especially at the distal ends of the lava flows where they contact the basin floor (Fig. 1). We therefore interpret the EAVS to be a modern analog for the formation of seaward dipping reflectors (SDRs; Planke et al., 2000). Studies of magmatic passive margins typically show the presence of SDRs, which are interpreted to be thick accumulations of basaltic lava flows interbedded with evaporites deposited just prior to seafloor spreading (White et al., 2008; Gernon et al., 2016). SDRs are interpreted to form from elevated asthenospheric melt supply induced by mechanisms such as rapid plate stretching and small-scale convection at the point of continental breakup (e.g., Ligi et al., 2011; Bastow & Keir, 2011).

# 6   CONCLUSIONS

We produced the first detailed geological map and relative chronology of the Alu-Dalafilla and Borale volcanic centres within the EAVS. We also performed petrological observation and major element geochemical analysis to provide some understanding of the areas evolution over time. Our main findings were as follows.

- All three volcanic centres (Alu, Dalafilla and Borale) are dominated by fissure eruptions that dominantly produce basaltic lavas.
- Volcanic products of Stage 3 characterised by intermediate and felsic compositions (56-71 wt % $SiO_2$) were erupted from the volcanic centres of Alu, Dalafilla and Borale, and (with the exception of the original rift floor basalts) were the largest eruptive phases in the history of these complexes.
- Basalts (48-50.5 wt% $SiO_2$) of Stages 1, 2 and 4 were sourced from fissures and scoria cones off-axis. Stages 2 and 4 had volumes <0.08 km$^3$, with the volume erupting from fissures decreasing over time in the area.
- Geochemical modelling carried out on whole rock samples indicate that all compositions may be explained through fractional crystallisation, with the exception of five samples, which require plagioclase accumulation.
- The presence of radial fissures and dykes at Alu alongside curvilinear faults at Borale indicate periods of uplift and subsidence relating to changing magma pressure within the system.
- We suggest a plumbing structure model consisting of a dyke dominated system off-rift which feeds the fissures, and a stacked sill dominated system beneath the volcanic centres allowing more extensive fractional crystallisation to occur.
- We propose that the EAVS is a volcanic segment situated on a highly evolved continental rift, which is experiencing a period of elevated melt flux prior to the onset of seafloor spreading, typical of that observed globally during continental breakup.

Overall, we show that that while fissure style eruptions are typical of this rifting segment, occasionally felsic eruptions occur, which pose different hazards.

# 7   ACKNOWLEDGEMENTS

Author Statement

**Emma J. Watts:** Writing – Original Draft, Methodology, Visualization, Investigation.
**Thomas M. Gernon:** Conceptualization, Supervision, Writing – Review & Editing.
**Rex Taylor:** Conceptualization, Supervision, Resources, Software, Writing – Review & Editing.
**Derek Keir:** Conceptualization, Supervision, Resources, Writing – Review & Editing.
**Melanie Siegburg:** Supervision, Writing – Review & Editing.
**Jasmin Jarman:** Investigation, Writing – Review & Editing.
**Carolina Pagli:** Resources, Writing – Review & Editing.
**Anna Gioncada:** Resources, Writing – Review & Editing.

 **Declaration of interests**
The authors declare that they have no known competing financial interests or personal relationships that could have appeared to influence the work reported in this paper.
The authors declare the following financial interests/personal relationships which may be considered as potential competing interests:

# 8   REFERENCES

Acocella, V., 2006. Regional and local tectonics at Erta Ale caldera, Afar (Ethiopia). Journal of Structural Geology 28, pp.1808-1820. doi:10.1016/j.jsg.2006.06.014

Anderson, E.M., 1937. Cone-sheets and ring-dykes: the dynamical explanation. *Bulletin Volcanologique*, *1*(1), pp.35-40. doi:10.1007/BF03028041

Ayalew, D., Pik, R., Bellahsen, N., France, L. and Yirgu, G., 2019. Differential fractionation of rhyolites during the course of crustal extension, Western Afar (Ethiopian rift). *Geochemistry, Geophysics, Geosystems*, *20*(2), pp.571-593. doi:10.1029/2018GC007446

Barberi, F. & Varet, J., 1970. The Erta Ale volcanic range (Danakil depression, northern Afar, Ethiopia). Bulletin Volcanologique 34, pp.848-917. doi:10.1007/BF02596805

Barberi, F., Borsi, S., Ferrara, G., Marinelli, G. & Varet, J., 1970. Relations between tectonics and magmatology in the northern Danakil Depression (Ethiopia). Philosophical Transactions for the Royal Society of London. Series A, Mathematical and Physical Sciences pp.293-311.

Barberi, F., Tazieff, H. and Varet, J., 1972. Volcanism in the Afar depression: its tectonic and magmatic significance. *Tectonophysics*, *15*(1-2), pp.19-29. doi:10.1016/0040-1951(72)90046-7

Barberi, F., Chedeville, E., Faure, H., Marinelli, G., Santacroce, R., Tazieff, H. and Varet, J., 1973. Geology of Northern Afar (Ethiopia).

[dataset] Barrat, J., Fourcade, S., Jahn, B., Cheminee, J. & Capdevila, R., 1998. Isotope (Sr, Nd, Pb, O) and trace-element geochemistry of volcanics from the Erta'Ale range (Ethiopia). Journal of Volcanology and Geothermal Research 80, pp. 85-100. doi:10.1016/S0377-0273(97)00016-4

BAS, M.L., Maitre, R.L., Streckeisen, A., Zanettin, B. and IUGS Subcommission on the Systematics of Igneous Rocks, 1986. A chemical classification of volcanic rocks based on the total alkali-silica diagram. *Journal of petrology*, *27*(3), pp.745-750. doi:10.1093/petrology/27.3.745

Bastow, I.D. and Keir, D., 2011. The protracted development of the continent–ocean transition in Afar. *Nature Geoscience*, *4*(4), pp.248-250. doi:10.1038/ngeo1095

Bennett, E.N., Lissenberg, C.J. and Cashman, K.V., 2019. The significance of plagioclase textures in mid-ocean ridge basalt (Gakkel Ridge, Arctic Ocean). *Contributions to Mineralogy and Petrology*, *174*(6), p.49. doi:10.1007/s00410-019-1587-1

Beyene, A. and Abdelsalam, M.G., 2005. Tectonics of the Afar Depression: A review and synthesis. *Journal of African Earth Sciences*, *41*(1-2), pp.41-59. doi:10.1016/j.jafrearsci.2005.03.003

Bilham, R., Bendick, R., Larson, K., Mohr, P., Braun, J., Tesfaye, S. and Asfaw, L., 1999. Secular and tidal strain across the Main Ethiopian Rift. *Geophysical Research Letters*, *26*(18), pp.2789-2792. doi:10.1029/1998GL005315

Bizouard, H., Barberi, F. and Varet, J., 1980. Mineralogy and petrology of Erta Ale and Boina volcanic series, Afar rift, Ethiopia. *Journal of Petrology*, *21*(2), pp.401-436. doi:10.1093/petrology/21.2.401

Bonatti, E., Emiliani, C., Ostlund, G. and Rydell, H., 1971. Final desiccation of the Afar rift, Ethiopia. *Science*, *172*(3982), pp.468-469. doi:10.1126/science.172.3982.468

Carbotte, S.M., Smith, D.K., Cannat, M. and Klein, E.M., 2016. Tectonic and magmatic segmentation of the Global Ocean Ridge System: a synthesis of observations. *Geological Society, London, Special Publications*, *420*(1), pp.249-295. doi:10.1144/SP420.5

CNR-CNRS, 1975. *Geological Maps of Afar: 1, Northern Afar (1971); 2, Central and Southern Afar* (1975). La Celle St Cloud, France: Geotechnip.

Colman, A., Sinton, J.M., White, S.M., McClinton, J.T., Bowles, J.A., Rubin, K.H., Behn, M.D., Cushman, B., Eason, D.E., Gregg, T.K. and Grönvold, K., 2012. Effects of variable magma supply on mid-ocean ridge eruptions: Constraints from mapped lava flow fields along the Galápagos Spreading Center. *Geochemistry, Geophysics, Geosystems*, *13*(8). doi:10.1029/2012GC004163

Corti, G., 2009. Continental rift evolution: from rift initiation to incipient break-up in the Main Ethiopian Rift, East Africa. *Earth-Science Reviews*, *96*(1-2), pp.1-53. doi:10.1016/j.earscirev.2009.06.005

Deniel, C., Vidal, P., Coulon, C., Vellutini, P.J. and Piguet, P., 1994. Temporal evolution of mantle sources during continental rifting: the volcanism of Djibouti (Afar). *Journal of Geophysical Research: Solid Earth*, *99*(B2), pp.2853-2869. doi:10.1029/93JB02576

Dungan, M.A. and Rhodes, J.M., 1978. Residual glasses and melt inclusions in basalts from DSDP Legs 45 and 46: evidence for magma mixing. *Contributions to Mineralogy and Petrology*, *67*(4), pp.417-431. doi:10.1007/BF00383301

Ebinger, C.J. and Casey, M., 2001. Continental breakup in magmatic provinces: An Ethiopian example. *Geology*, *29*(6), pp.527-530. doi:10.1130/0091-7613(2001)029<0527:CBIMPA>2.0.CO;2

Ebinger, C.J. and Hayward, N.J., 1996. Soft plates and hot spots: Views from Afar. *Journal of Geophysical Research: Solid Earth*, *101*(B10), pp.21859-21876. doi:10.1029/96JB02118

Ebinger, C.J., Keir, D., Ayele, A., Calais, E., Wright, T.J., Belachew, M., Hammond, J.O., Campbell, E. and Buck, W.R., 2008. Capturing magma intrusion and faulting processes during continental rupture: seismicity of the Dabbahu (Afar) rift. *Geophysical Journal International*, *174*(3), pp.1138-1152. doi:10.1111/j.1365-246X.2008.03877.x

Ebinger, C.J., Keir, D., Bastow, I.D., Whaler, K., Hammond, J.O., Ayele, A., Miller, M.S., Tiberi, C. and Hautot, S., 2017. Crustal structure of active deformation zones in Africa: Implications for global crustal processes. *Tectonics*, *36*(12), pp.3298-3332. doi:10.1002/2017TC004526

Field, L., Barnie, T., Blundy, J., Brooker, R.A., Keir, D., Lewi, E. and Saunders, K., 2012a. Integrated field, satellite and petrological observations of the November 2010 eruption of Erta Ale. *Bulletin of Volcanology*, *74*(10), pp.2251-2271. doi:10.1007/s00445-012-0660-7

Field, L., Blundy, J., Brooker, R.A., Wright, T. and Yirgu, G., 2012b. Magma storage conditions beneath Dabbahu Volcano (Ethiopia) constrained by petrology, seismicity and satellite geodesy. *Bulletin of Volcanology*, *74*(5), pp.981-1004. doi:10.1007/s00445-012-0580-6

Field, L., Blundy, J., Calvert, A. and Yirgu, G., 2013. Magmatic history of Dabbahu, a composite volcano in the Afar Rift, Ethiopia. *Bulletin*, *125*(1-2), pp.128-147.

Ferguson, D.J., Calvert, A.T., Pyle, D.M., Blundy, J.D., Yirgu, G. and Wright, T.J., 2013. Constraining timescales of focused magmatic accretion and extension in the Afar crust using lava geochronology. *Nature communications*, *4*(1), pp.1-6. doi:10.1038/ncomms2410

[dataset] Feyissa, D.H., Shinjo, R., Kitagawa, H., Meshesha, D. and Nakamura, E., 2017. Petrologic and geochemical characterization of rift-related magmatism at the northernmost Main Ethiopian Rift: Implications for plume-lithosphere interaction and the evolution of rift mantle sources. *Lithos*, *282*, pp.240-261. doi:10.1016/j.lithos.2017.03.011

Gernon, T.M., Hincks, T.K., Tyrrell, T., Rohling, E.J. and Palmer, M.R., 2016. Snowball Earth ocean chemistry driven by extensive ridge volcanism during Rodinia breakup. *Nature Geoscience*, *9*(3), pp.242-248. doi:10.1038/ngeo2632

Gleeson, M.L., Stock, M.J., Pyle, D.M., Mather, T.A., Hutchison, W., Yirgu, G. and Wade, J., 2017. Constraining magma storage conditions at a restless volcano in the Main Ethiopian Rift using phase equilibria models. *Journal of Volcanology and Geothermal Research*, *337*, pp.44-61. doi:10.1016/j.jvolgeores.2017.02.026

Global Volcanism Program, 2013. Volcanoes of the World, v. 4.8.6. Venzke, E (ed.). Smithsonian Institution. Downloaded 01 Mar 2020. doi:10.5479/si.GVP.VOTW4-2013

Gualda, G.A. and Ghiorso, M.S., 2015. MELTS_Excel: A Microsoft Excel-based MELTS interface for research and teaching of magma properties and evolution. *Geochemistry, Geophysics, Geosystems*, *16*(1), pp.315-324. doi:10.1002/2014GC005545

Hagos, M., Koeberl, C. and de Vries, B.V.W., 2016. The Quaternary volcanic rocks of the northern Afar Depression (northern Ethiopia): Perspectives on petrology, geochemistry, and tectonics. *Journal of African Earth Sciences*, *117*, pp.29-47. doi:10.1016/j.jafrearsci.2015.11.022

Hammond, J.O., Kendall, J.M., Stuart, G.W., Keir, D., Ebinger, C., Ayele, A. and Belachew, M., 2011. The nature of the crust beneath the Afar triple junction: Evidence from receiver functions. *Geochemistry, Geophysics, Geosystems*, *12*(12). doi:10.1029/2011GC003738

Hayward, N.J. and Ebinger, C.J., 1996. Variations in the along-axis segmentation of the Afar Rift system. *Tectonics*, *15*(2), pp.244-257. doi:10.1029/95TC02292

Hofmann, C., Courtillot, V., Feraud, G., Rochette, P., Yirgu, G., Ketefo, E. and Pik, R., 1997. Timing of the Ethiopian flood basalt event and implications for plume birth and global change. *Nature*, *389*(6653), pp.838-841. doi:10.1038/39853

Hofstetter, R. and Beyth, M., 2003. The Afar Depression: interpretation of the 1960–2000 earthquakes. *Geophysical Journal International*, *155*(2), pp.715-732. doi:10.1046/j.1365-246X.2003.02080.x

[dataset] Hutchison, W., Pyle, D.M., Mather, T.A., Yirgu, G., Biggs, J., Cohen, B.E., Barfod, D.N. and Lewi, E., 2016. The eruptive history and magmatic evolution of Aluto volcano: new insights into silicic peralkaline volcanism in the Ethiopian rift. *Journal of Volcanology and Geothermal Research*, *328*, pp.9-33. doi:10.1016/j.jvolgeores.2016.09.010

Hutchison, W., Mather, T.A., Pyle, D.M., Boyce, A.J., Gleeson, M.L., Yirgu, G., Blundy, J.D., Ferguson, D.J., Vye-Brown, C., Millar, I.L. and Sims, K.W., 2018. The evolution of magma during continental rifting: New constraints from the isotopic and trace element signatures of silicic magmas from Ethiopian volcanoes. *Earth and Planetary Science Letters*, *489*, pp.203-218. doi:10.1016/j.epsl.2018.02.027

Illsley-Kemp, F., Keir, D., Bull, J.M., Gernon, T.M., Ebinger, C., Ayele, A., Hammond, J.O., Kendall, J.M., Goitom, B. and Belachew, M., 2018a. Seismicity during continental breakup in the Red Sea rift of northern Afar. *Journal of Geophysical Research: Solid Earth*, *123*(3), pp.2345-2362. doi:10.1002/2017JB014902

Illsley-Kemp, F. M. Crustal Processes Associated with the Final Stages of Continental Rifting in Northern Afar. Ph.D. thesis, University of Southampton (2018b).

Jokat, W., Ritzmann, O., Schmidt-Aursch, M.C., Drachev, S., Gauger, S. and Snow, J., 2003. Geophysical evidence for reduced melt production on the Arctic ultraslow Gakkel mid-ocean ridge. *Nature*, *423*(6943), pp.962-965. doi:10.1038/nature01706

Keir, D., Hamling, I.J., Ayele, A., Calais, E., Ebinger, C., Wright, T.J., Jacques, E., Mohamed, K., Hammond, J.O., Belachew, M. and Baker, E., 2009. Evidence for focused magmatic accretion at segment centers from lateral dike injections captured beneath the Red Sea rift in Afar. *Geology*, *37*(1), pp.59-62. doi:10.1130/G25147A.1

Keir, D., 2014. Magmatism and deformation during continental breakup. *Astronomy & Geophysics*, *55*(5), pp.5-18. doi:10.1093/astrogeo/atu213

Kendall, J.M., Stuart, G.W., Ebinger, C.J., Bastow, I.D. and Keir, D., 2005. Magma-assisted rifting in Ethiopia. *Nature*, *433*(7022), pp.146-148. doi:10.1038/nature03161

Kresten, P., 1980. The Alnö complex: tectonics of dyke emplacement. *Lithos*, *13*(2), pp.153-158. doi:10.1016/0024-4937(80)90016-X

Lahitte, P., Gillot, P.Y. and Courtillot, V., 2003. Silicic central volcanoes as precursors to rift propagation: the Afar case. *Earth and Planetary Science Letters*, *207*(1-4), pp.103-116. doi:10.1016/S0012-821X(02)01130-5

Lalou, C., Nguyen, H.V., Faure, H. and Moreira, L., 1970. Datation par la méthode Uranium—Thorium des hauts niveaux de coraux de la dépression de l'Afar (Ethiopie). *Rev Géo Phys Géol Dyn*, *12*, pp.3-8.

Leroy, S., Razin, P., Autin, J., Bache, F., d'Acremont, E., Watremez, L., Robinet, J., Baurion, C., Denèle, Y., Bellahsen, N. and Lucazeau, F., 2012. From rifting to oceanic spreading in the Gulf of Aden: a synthesis. *Arabian Journal of Geosciences*, *5*(5), pp.859-901. doi:10.1007/s12517-011-0475-4

Lewi, E., Keir, D., Birhanu, Y., Blundy, J., Stuart, G., Wright, T. and Calais, E., 2016. Use of a high-precision gravity survey to understand the formation of oceanic crust and the role of melt at the southern Red Sea rift in Afar, Ethiopia. *Geological Society, London, Special Publications*, *420*(1), pp.165-180. doi:10.1144/SP420.13

Ligi, M., Bonatti, E., Tontini, F.C., Cipriani, A., Cocchi, L., Schettino, A., Bortoluzzi, G., Ferrante, V., Khalil, S., Mitchell, N.C. and Rasul, N., 2011. Initial burst of oceanic crust accretion in the Red Sea due to edge-driven mantle convection. *Geology*, *39*(11), pp.1019-1022. doi:10.1130/G32243.1

Magee, C., Bastow, I.D., van Wyk de Vries, B., Jackson, C.A.L., Hetherington, R., Hagos, M. and Hoggett, M., 2017. Structure and dynamics of surface uplift induced by incremental sill emplacement. *Geology*, *45*(5), pp.431-434. doi:10.1130/G38839.1

Maguire, P.K.H., Keller, G.R., Klemperer, S.L., Mackenzie, G.D., Keranen, K., Harder, S., O'Reilly, B., Thybo, H., Asfaw, L., Khan, M.A. and Amha, M., 2006. Crustal structure of the northern Main

Ethiopian Rift from the EAGLE controlled-source survey; a snapshot of incipient lithospheric break-up. *Geological Society, London, Special Publications*, *259*(1), pp.269-292. doi:10.1144/GSL.SP.2006.259.01.21

Makris, J. and Ginzburg, A., 1987. The Afar Depression: transition between continental rifting and sea-floor spreading. *Tectonophysics*, *141*(1-3), pp.199-214. doi:10.1016/0040-1951(87)90186-7

McClusky, S., Reilinger, R., Ogubazghi, G., Amleson, A., Healeb, B., Vernant, P., Sholan, J., Fisseha, S., Asfaw, L., Bendick, R. and Kogan, L., 2010. Kinematics of the southern Red Sea–Afar Triple Junction and implications for plate dynamics. *Geophysical Research Letters*, *37*(5). doi:10.1029/2009GL041127

McKenzie, D.P., Davies, D. and Molnar, P., 1970. Plate tectonics of the Red Sea and east Africa. *Nature*, *226*(5242), pp.243-248. doi:10.1038/226243a0

Moore, C., Wright, T., Hooper, A. and Biggs, J., 2019. The 2017 Eruption of Erta'Ale Volcano, Ethiopia: Insights Into the Shallow Axial Plumbing System of an Incipient Mid-Ocean Ridge. *Geochemistry, Geophysics, Geosystems*. doi:10.1029/2019GC008692

Nelson, S.T. and Montana, A., 1992. Sieve-textured plagioclase in volcanic rocks produced by rapid decompression. *American Mineralogist*, *77*(11-12), pp.1242-1249

Oppenheimer, C. and Francis, P.E.T.E.R., 1997. Remote sensing of heat, lava and fumarole emissions from Erta'Ale volcano, Ethiopia. *International Journal of Remote Sensing*, *18*(8), pp.1661-1692. doi:10.1080/014311697218043

Pagli, C., Mazzarini, F., Keir, D., Rivalta, E. and Rooney, T.O., 2015. Introduction: Anatomy of rifting: Tectonics and magmatism in continental rifts, oceanic spreading centers, and transforms. *Geosphere*, *11*(5), pp.1256-1261. doi:10.1130/GES01082.1

Pagli, C., Wright, T.J., Ebinger, C.J., Yun, S.H., Cann, J.R., Barnie, T. and Ayele, A., 2012. Shallow axial magma chamber at the slow-spreading Erta Ale Ridge. *Nature Geoscience*, *5*(4), pp.284-288. doi:10.1038/ngeo1414

[dataset] Peccerillo, A., Barberio, M.R., Yirgu, G., Ayalew, D., Barbieri, M.W.U.T.W. and Wu, T.W., 2003. Relationships between mafic and peralkaline silicic magmatism in continental rift settings: a petrological, geochemical and isotopic study of the Gedemsa volcano, central Ethiopian rift. *Journal of Petrology*, *44*(11), pp.2003-2032. doi:10.1093/petrology/egg068

Pik, R., Deniel, C., Coulon, C., Yirgu, G. and Marty, B., 1999. Isotopic and trace element signatures of Ethiopian flood basalts: evidence for plume–lithosphere interactions. *Geochimica et Cosmochimica Acta*, *63*(15), pp.2263-2279. doi:10.1016/S0016-7037(99)00141-6

Planke, S., Symonds, P.A., Alvestad, E. and Skogseid, J., 2000. Seismic volcanostratigraphy of large-volume basaltic extrusive complexes on rifted margins. *Journal of Geophysical Research: Solid Earth*, *105*(B8), pp.19335-19351. doi:10.1029/1999JB900005

Rooney, T., Furman, T., Bastow, I., Ayalew, D. and Yirgu, G., 2007. Lithospheric modification during crustal extension in the Main Ethiopian Rift. *Journal of Geophysical Research: Solid Earth*, *112*(B10). doi:10.1029/2006JB004916

Rooney, T.O., Herzberg, C. and Bastow, I.D., 2012. Elevated mantle temperature beneath East Africa. *Geology*, *40*(1), pp.27-30. doi:10.1130/G32382.1

Schouten, H., Dick, H.J. and Klitgord, K.D., 1987. Migration of mid-ocean-ridge volcanic segments. *Nature*, *326*(6116), pp.835-839. doi:10.1038/326835a0

Siegburg, M., Bull, J.M., Nixon, C.W., Keir, D., Gernon, T.M., Corti, G., Abebe, B., Sanderson, D.J. and Ayele, A., 2020. Quantitative constraints on faulting and fault slip-rates in the northern Main Ethiopian Rift. *Tectonics*, p.e2019TC006046. doi:10.1029/2019TC006046

Stevens, N.F., Wadge, G. and Murray, J.B., 1999. Lava flow volume and morphology from digitised contour maps: a case study at Mount Etna, Sicily. *Geomorphology*, *28*(3-4), pp.251-261. doi:10.1016/S0169-555X(98)00115-9

Thurmond, A.K., Abdelsalam, M.G. and Thurmond, J.B., 2006. Optical-radar-DEM remote sensing data integration for geological mapping in the Afar Depression, Ethiopia. *Journal of African Earth Sciences*, *44*(2), pp.119-134. doi:10.1016/j.jafrearsci.2005.10.006

Venzke, E., Sennert, S.K. and Wunderman, R., 2009. Reports from the Smithsonian's Global Volcanism Network, October 2008. *Bulletin of Volcanology*, *71*(5), pp.589-590. doi:10.1007/s00445-009-0269-7

Vidal, P., Deniel, C., Vellutini, P.J., Piguet, P., Coulon, C., Vincent, J. and Audin, J., 1991. Changes of mantle sources in the course of a rift evolution: the Afar case. *Geophysical Research Letters*, *18*(10), pp.1913-1916. doi:10.1029/91GL02006

White, R. and McKenzie, D., 1989. Magmatism at rift zones: the generation of volcanic continental margins and flood basalts. *Journal of Geophysical Research: Solid Earth*, *94*(B6), pp.7685-7729. doi:10.1029/JB094iB06p07685

White, R.S., Smith, L.K., Roberts, A.W., Christie, P.A.F. and Kusznir, N.J., 2008. Lower-crustal intrusion on the North Atlantic continental margin. *Nature*, *452*(7186), pp.460-464.

Wolfenden, E., Ebinger, C., Yirgu, G., Deino, A. and Ayalew, D., 2004. Evolution of the northern Main Ethiopian rift: birth of a triple junction. *Earth and Planetary Science Letters*, *224*(1-2), pp.213-228. doi:10.1016/j.epsl.2004.04.022

Wolfenden, E., Ebinger, C., Yirgu, G., Renne, P.R. and Kelley, S.P., 2005. Evolution of a volcanic rifted margin: Southern Red Sea, Ethiopia. *Geological Society of America Bulletin*, *117*(7-8), pp.846-864. doi:10.1130/B25516.1

Wright, T.J., Ebinger, C., Biggs, J., Ayele, A., Yirgu, G., Keir, D. and Stork, A., 2006. Magma-maintained rift segmentation at continental rupture in the 2005 Afar dyking episode. *Nature*, *442*(7100), pp.291-294. doi:10.1038/nature04978

Wright, T.J., Sigmundsson, F., Pagli, C., Belachew, M., Hamling, I.J., Brandsdóttir, B., Keir, D., Pedersen, R., Ayele, A., Ebinger, C. and Einarsson, P., 2012. Geophysical constraints on the dynamics of spreading centres from rifting episodes on land. *Nature Geoscience*, *5*(4), pp.242-250. doi:10.1038/ngeo1428

Xu, W., Rivalta, E. and Li, X., 2017. Magmatic architecture within a rift segment: Articulate axial magma storage at Erta Ale volcano, Ethiopia. *Earth and Planetary Science Letters*, *476*, pp.79-86. doi:10.1016/j.epsl.2017.07.051

Yirgu, G., Ebinger, C.J. and Maguire, P.K.H., 2006. The afar volcanic province within the East African Rift System: introduction. *Geological Society, London, Special Publications*, *259*(1), pp.1-6. doi:10.1144/GSL.SP.2006.259.01.01

Zwaan, F., Corti, G., Sani, F., Keir, D., Muluneh, A., Illsley-Kemp, F. and Papini, M., 2020. Structural analysis of the Western Afar Margin, East Africa: evidence for multiphase rotational rifting. *Tectonics*, p.e2019TC006043. doi:10.1029/2019TC006043

**Highlights for Manuscript [VOLGEO_2020_300]: Evolution of the Alu-Dalafilla and Borale Volcanoes, Afar, Ethiopia.**

- Alu-Dalafilla and Borale have had four main eruptive stages in their evolution.
- Activity is dominated by fissure eruptions producing basaltic lavas.

- Intermediate and felsic activity occurred at all three volcanic centres.
- Modelling shows compositions can be achieved through fractional crystallisation.
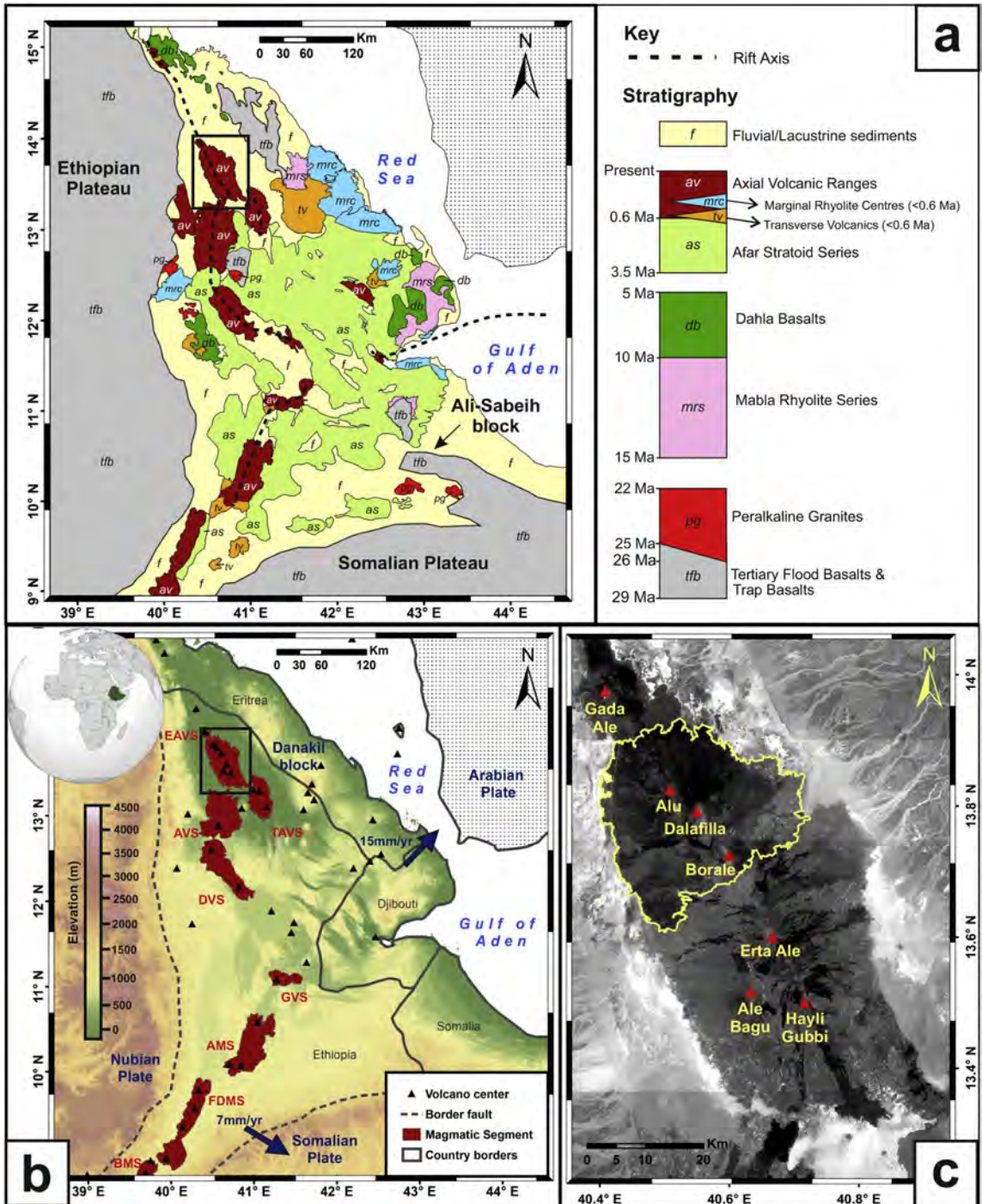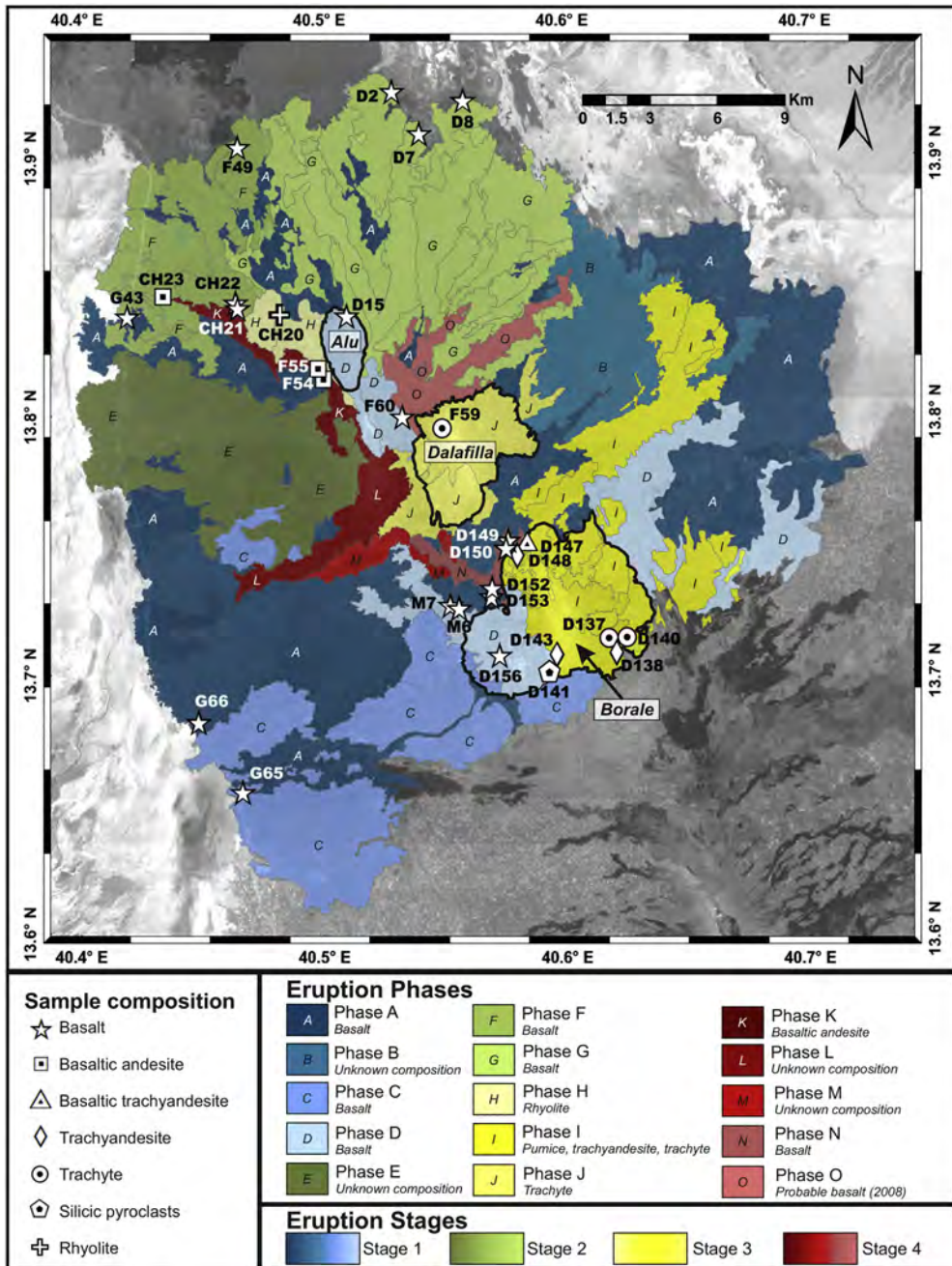- Radial fissures, dykes and curvilinear faults suggest changing magma pressures.

Figure 1

Figure 2

Figure 3
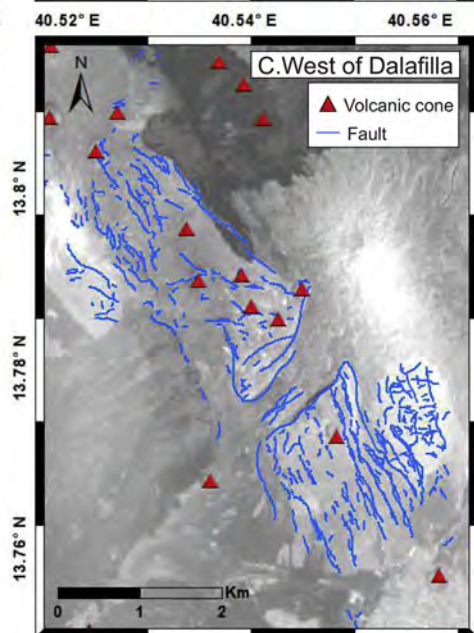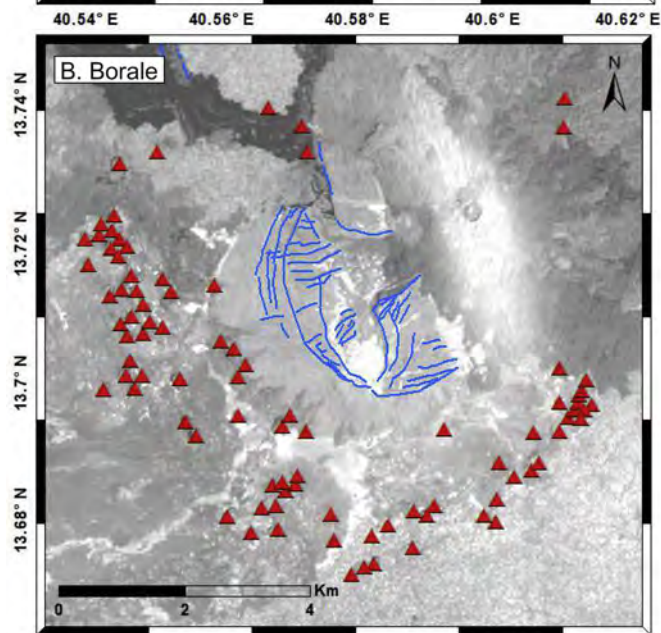
Figure 4
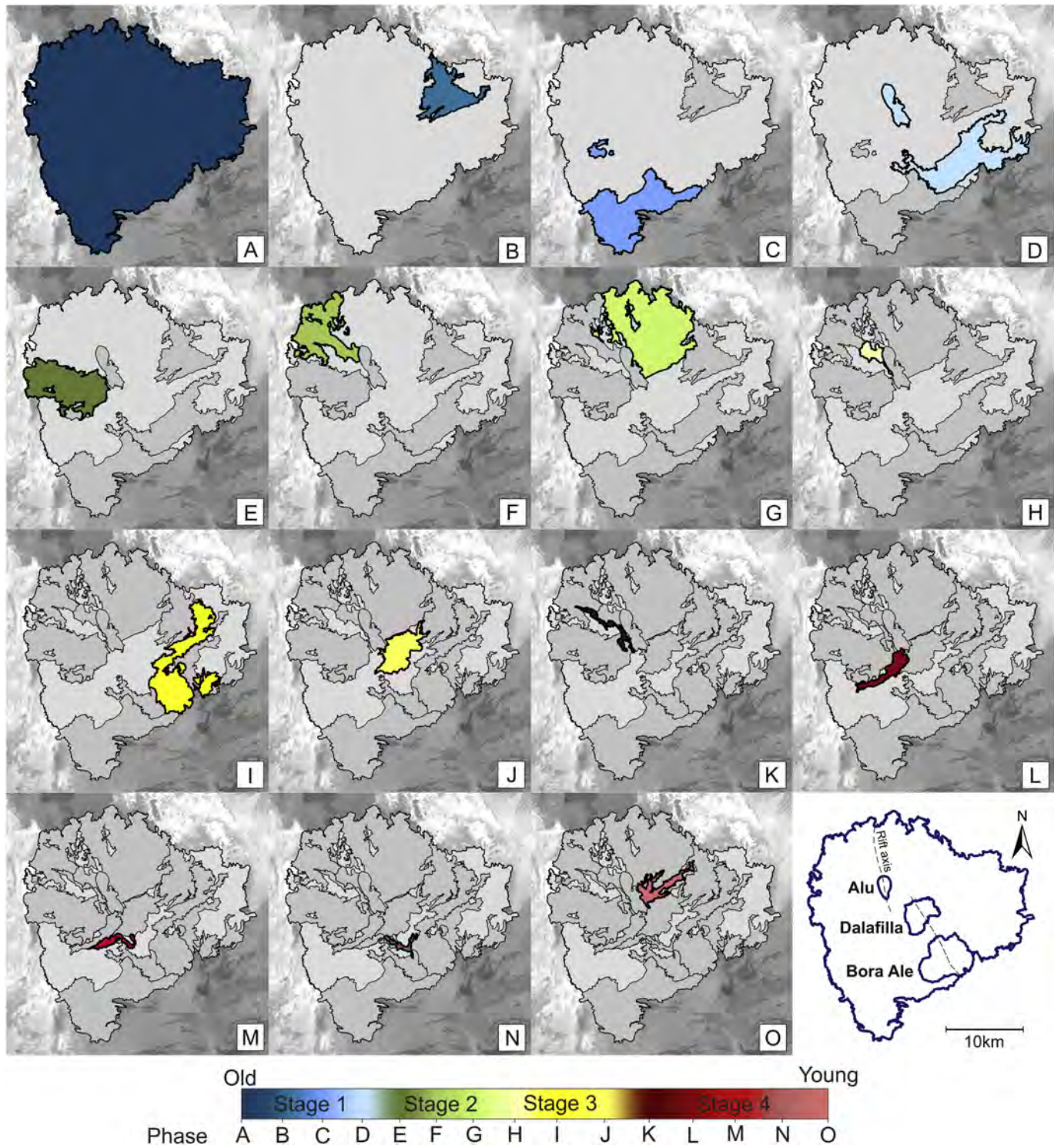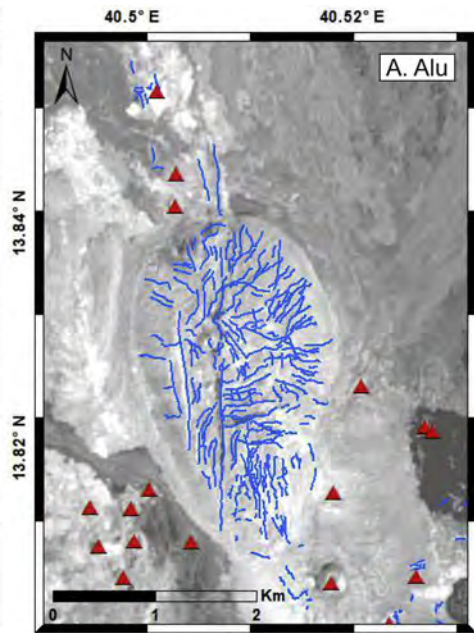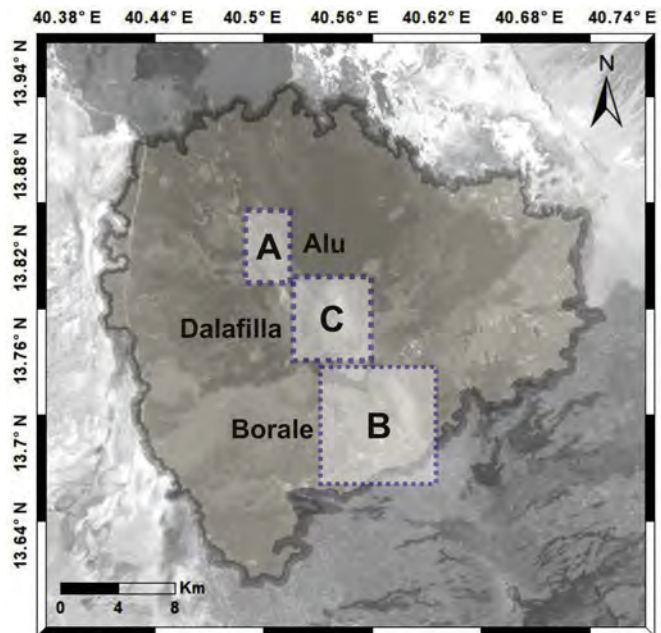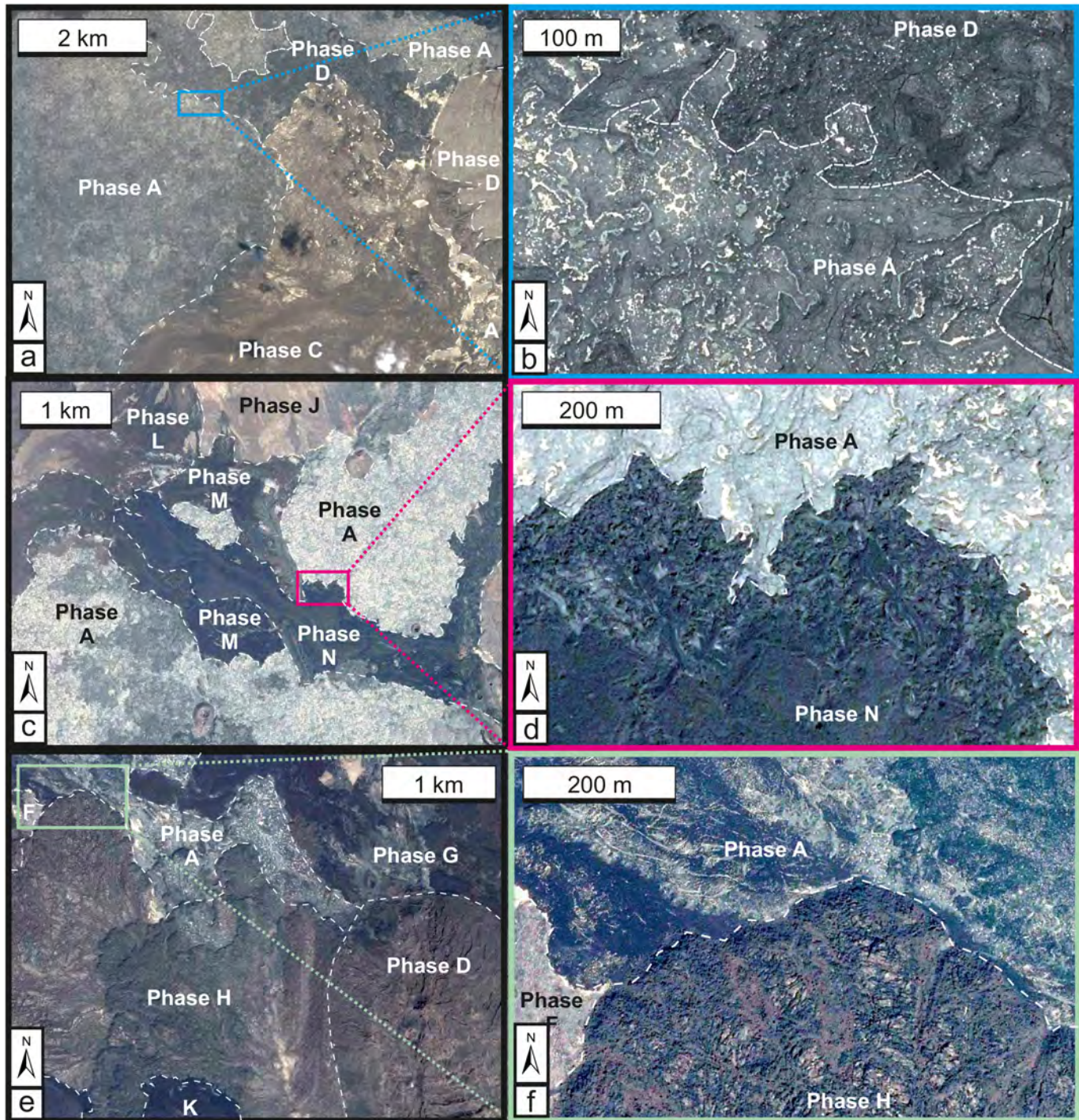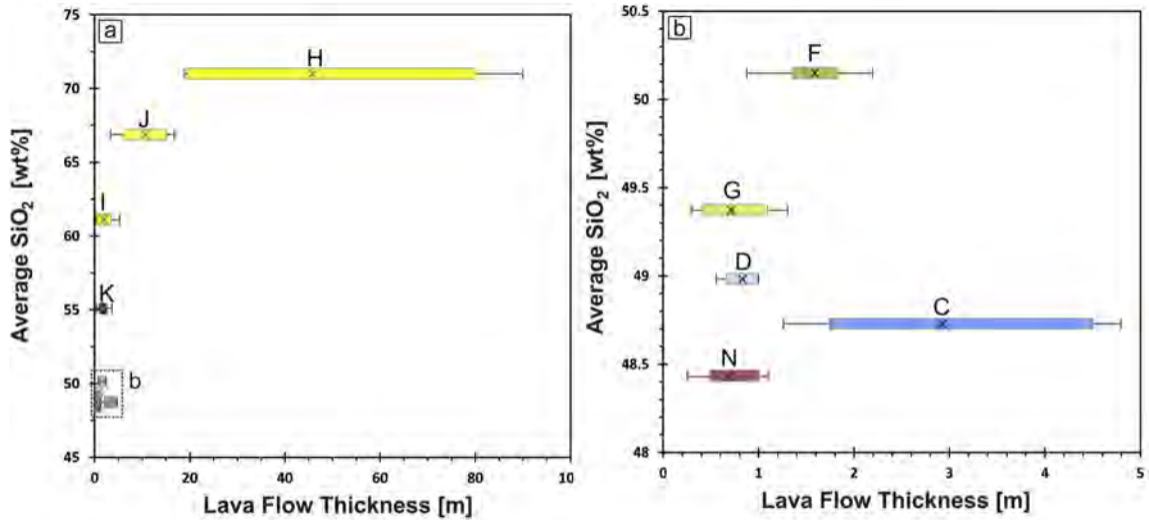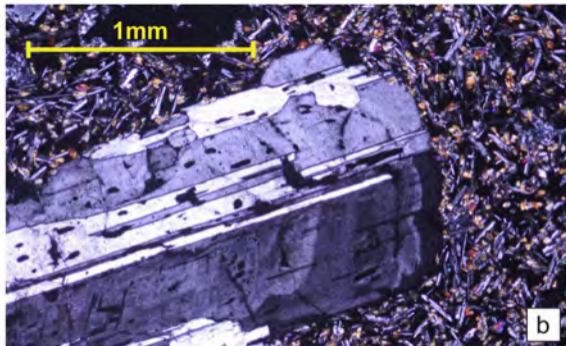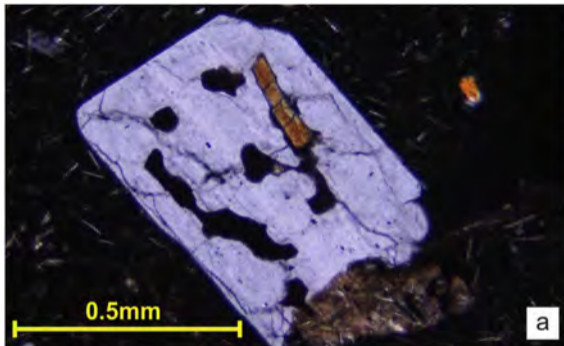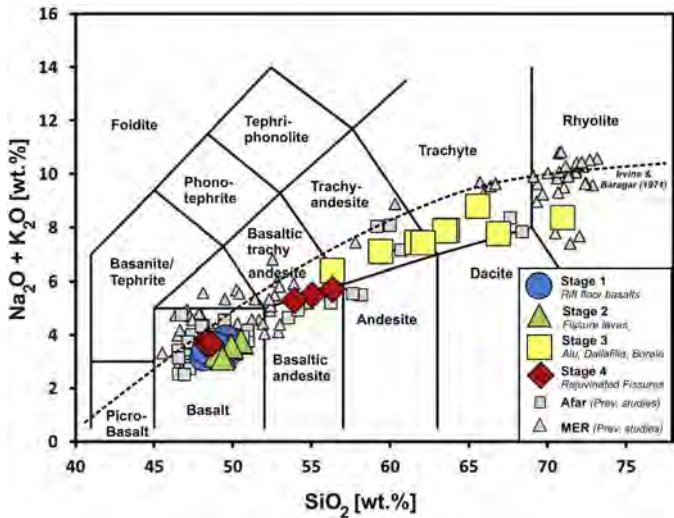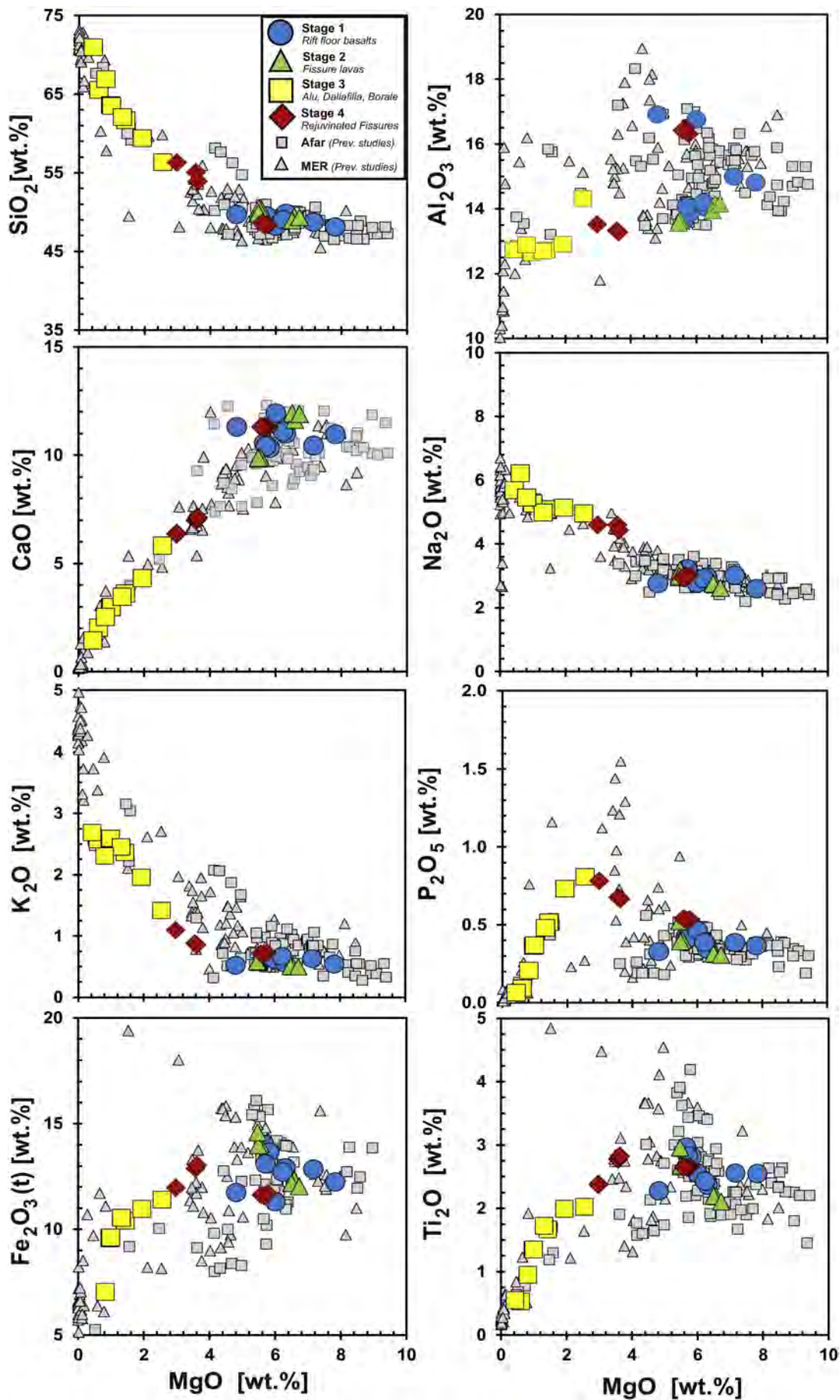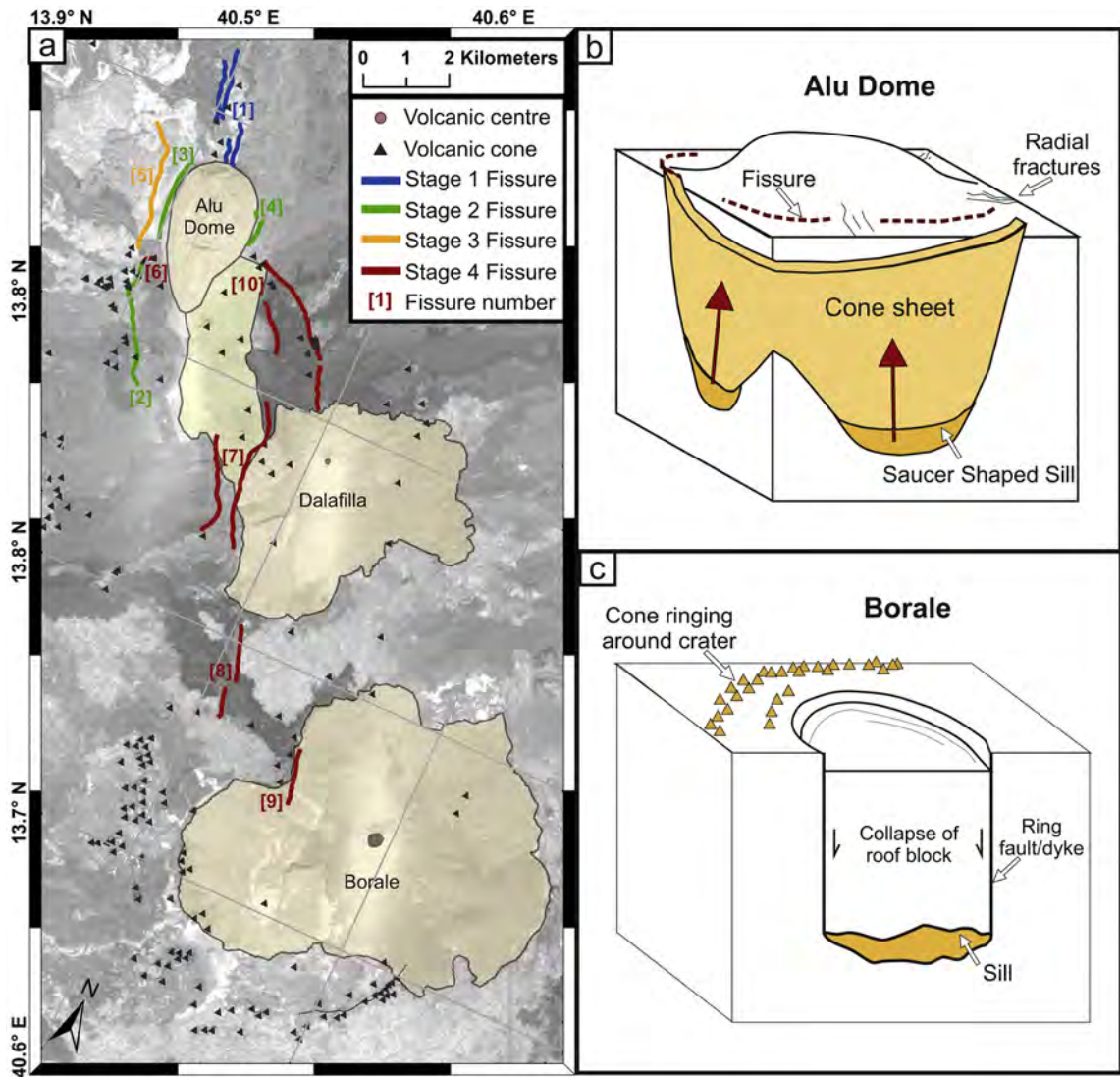
Figure 5

Figure 6

Figure 7

Figure 8

Figure 9

Figure 10

Figure 11